Draft version October 10, 2021
Typeset using LaTeX **twocolumn** style in AASTeX62

arXiv:2008.02283v3 [astro-ph.HE] 5 Oct 2020

Probing the Milky Way's Dark Matter Halo for the 3.5 keV Line

Dominic Sicilian,[1,2] Nico Cappelluti,[1] Esra Bulbul,[2,3] Francesca Civano,[2] Massimo Moscetti,[1,4] and Christopher S. Reynolds[5]

[1] *University of Miami, Coral Gables, FL*
[2] *Center for Astrophysics | Harvard & Smithsonian, 60 Garden Street, Cambridge, MA*
[3] *Max Planck Institute for Extraterrestrial Physics, Garching bei München, Bayern, Germany*
[4] *Palmer Trinity School, Miami, FL*
[5] *Institute of Astronomy, University of Cambridge, Madingley Road, Cambridge CB3 OHA, UK*

ABSTRACT

We present a comprehensive search for the 3.5 keV line, using ∼51 Ms of archival *Chandra* observations peering through the Milky Way's Dark Matter Halo from across the entirety of the sky, gathered via the *Chandra* Source Catalog Release 2.0. We consider the data's radial distribution, organizing observations into four data subsets based on angular distance from the Galactic Center. All data is modeled using both background-subtracted and background-modeled approaches to account for the particle instrument background, demonstrating statistical limitations of the currently-available ∼1 Ms of particle background data. A non-detection is reported in the total data set, allowing us to set an upper-limit on 3.5 keV line flux and constrain the sterile neutrino dark matter mixing angle. The upper-limit on $\sin^2(2\theta)$ is 2.58×10^{-11} (though systematic uncertainty may increase this by a factor of ∼2), corresponding to the upper-limit on 3.5 keV line flux of 2.34×10^{-7} ph s^{-1} cm^{-2}. These limits show consistency with recent constraints and several prior detections. Non-detections are reported in all radial data subsets, allowing us to constrain the spatial profile of 3.5 keV line intensity, which does not conclusively differ from Navarro-Frenk-White predictions. Thus, while offering heavy constraints, we do not entirely rule out the sterile neutrino dark matter scenario or the more general decaying dark matter hypothesis for the 3.5 keV line. We have also used the non-detection of any unidentified emission lines across our continuum to further constrain the sterile neutrino parameter space.

1. INTRODUCTION

Since its discovery (Zwicky 1933; Zwicky 1937), dark matter has been shown by numerous observations to be the Universe's dominant source of gravity and composed of undiscovered, non-baryonic material (Rubin & Ford 1970; Rubin et al. 1980; Clowe et al. 2006). Its nature and composition, however, remain unknown since the Standard Model does not offer any viable dark matter candidate (Boyarsky et al. 2019).

The solution to the dark matter problem could lie in neutrino cosmology. The three flavors of Standard Model neutrinos are massless and display only left-handed chirality. It is now known that neutrinos oscillate between flavors and therefore are not massless (Kajita 1999; McDonald 2002), in contrast to the Standard Model, and the probability of oscillation between flavors can be described by the mixing angle, θ (Pal & Wolfenstein 1982).

d.sicilian@umiami.edu

There is currently no explanation for the collective phenomenon of neutrino mass and oscillation, but a possible solution is the existence of hypothetical right-handed neutrinos (Dodelson & Widrow 1994; Abazajian et al. 2001a; Dolgov & Hansen 2002; Boyarsky et al. 2006b; Boyarsky et al. 2009b; Boyarsky et al. 2019). This could give neutrinos more direct correspondence to other known fermions—all of which can exhibit both right- and left-handed chirality—and resolve major problems in modern physics in addition to the neutrino mass problem. Since the weak interaction only couples to left-handed neutrinos (Drewes 2013, Pal & Wolfenstein 1982, etc.), right-handed neutrinos are referred to as sterile neutrinos due to their resulting lack of interaction via any forces besides gravity. In accordance with this naming convention, left-handed neutrinos are known as active neutrinos. Incidentally, the sterile neutrino could also solve the matter-antimatter asymmetry problem in the early Universe by giving rise to baryons through the process of leptogenesis (Asaka & Shaposhnikov 2005; Drewes & Garbrecht 2013; Drewes et al.

2016; Drewes et al. 2017; see Boyarsky et al. 2019 for further discussion).

The most relevant feature of the sterile neutrino to this work is its status as a dark matter candidate. Active neutrino masses are well known for being too small to constitute dark matter (Boyarsky et al. 2019), but sterile neutrinos can have much larger masses. In particular, sterile neutrino dark matter is thought to have mass in the keV range (Abazajian et al. 2001a; Abazajian et al. 2001b; Boyarsky et al. 2006a; Boyarsky et al. 2009a). Also, in a process separate from neutrino oscillation, any neutrino can decay into another neutrino with lower mass. The probability of this decay depends on the difference in masses of the neutrinos in question, so it rarely happens to active neutrinos (Pal & Wolfenstein 1982). However, the probability is considerably higher for a sterile neutrino with keV mass, with the decay rate given by:

$$\Gamma_\gamma(m_s,\theta) = 1.38\times10^{-29}s^{-1}\left(\frac{sin^2(2\theta)}{10^{-7}}\right)\left(\frac{m_s}{1keV}\right)^5 \quad (1)$$

where m_s is the sterile neutrino's mass and θ is the corresponding mixing angle (Pal & Wolfenstein 1982). This decay process results in an active neutrino and a photon with E = $m_s/2$, making the decay of a keV sterile neutrino observable by current X-ray telescopes such as *Chandra* (Abazajian et al. 2001a; Abazajian et al. 2001b).

When an unidentified emission line was discovered by Bulbul et al. (2014) near 3.5 keV at $\sim4.5\sigma$ significance in 73 stacked *XMM-Newton* galaxy clusters, in addition to Perseus and other clusters using *Chandra*, it served as the first possible experimental evidence of sterile neutrino dark matter decay. Soon after, the line was detected again with *XMM-Newton* at 3σ significance in M31 by Boyarsky et al. (2014), and in the Milky Way's Galactic Center at 5.7σ by Boyarsky et al. (2015). The line was later detected in the Perseus cluster at $\sim5\sigma$ using *Suzaku* by both Urban et al. (2015) and Franse et al. (2016). Recently, Cappelluti et al. (2018) detected a possible feature resembling the line at $\sim3\sigma$ in the *Chandra*-COSMOS Legacy Survey (CCLS) field and *Chandra* Deep Field South (CDFS), and another detection was made using archival *Chandra* observations of the Galactic bulge by Hofmann & Wegg (2019).

Due to the use of CCDs in the majority of 3.5 keV line detections, an unknown feature of CCDs has been hypothesized to be the source of the apparent emission. However, the line was also detected by *NuSTAR*'s cadmium zinc telluride (CdZnTe or CZT) detector in its observations of the Bullet cluster (Wik et al. 2014). The line was later detected again using *NuSTAR*, this time at 11σ by Neronov et al. (2016a) in the Milky Way's Dark Matter Halo, through the CCLS field and Extended *Chandra* Deep Field South (ECDFS). The *NuSTAR* detections have been questioned due to the proximity of 3.5 keV to the lower bound of *NuSTAR*'s sensitivity and the detection of the line by Perez et al. (2017) in a portion of observations where the FOV contains only Earth, suggesting that at least some part of the line in *NuSTAR* is instrumental.

Despite the many detections by various instruments in dark matter-dominated objects, some studies produced non-detections. These include stacked *Suzaku* clusters (Bulbul et al. 2016), *XMM-Newton* observations of the Draco dwarf galaxy (Ruchayskiy et al. 2016), *Hitomi* observations of the Perseus cluster (Hitomi Collaboration et al. 2017), and *XMM-Newton* observations of various galaxy clusters (Bhargava et al. 2020). The upper-limits provided by these non-detections are consistent with the original Bulbul et al. (2014) detection and do not rule out the decaying dark matter interpretation. Recently, Dessert et al. (2020) reported a non-detection in $\sim$31 Ms of archival *XMM-Newton* observations directed through the Milky Way's Dark Matter Halo. The Dessert et al. (2020) results, however, have been questioned in the X-ray astrophysics community due to the unconventional nature of the analysis, which considered an unusually small energy band and failed to properly account for known emission features at 3.3 keV and 3.68 keV, in addition to possible technical errors in data reduction (Abazajian 2020; Boyarsky et al. 2020). The fiducial constraints reported by Dessert et al. (2020) are in tension with the decaying dark matter interpretation of the 3.5 keV line, while supplemental upper-limits given in that work that account for the 3.3 keV and 3.68 keV emission features are marginally consistent with prior detections and are supported by Boyarsky et al. (2020). Both Boyarsky et al. (2020) and Abazajian (2020) show that the high dark matter density estimate adopted by Dessert et al. (2020) may relax even the supplemental upper-limit by up to a factor of $\sim$3. In particular, Dessert et al. (2020) uses a local dark matter density of 0.4 GeV cm^{-3}, much higher than strong empirical values such as the 0.28 GeV cm^{-3} found by Zhang et al. (2013). As discussed in Dessert et al. (2020a), these supplemental results still constrain the sterile neutrino dark matter scenario, but cannot rule out the hypothesis (Boyarsky et al. 2020).

Virtually all non-astrophysical explanations for the 3.5 keV line can be classified as arising from instrumental effects, but due to the variety of X-ray telescopes that have observed the line, this explanation is generally considered unlikely for the majority of detections. The

telescopes use different mirror coatings (either gold or iridium) and utilize different detectors, including CCDs and *NuSTAR*'s CZT detector, although as mentioned, the *NuSTAR* detections are likely instrumental. Another non-astrophysical interpretation could be statistical fluctuations, although this is also considered unlikely due to repeated high-significance detections. This prospect will be thoroughly addressed by the size of the data set used in this analysis.

Various non-dark matter, astrophysical explanations for the line have been discussed. Among these interpretations is contamination due to nearby K and Ar dielectric emission, both of which have been evaluated and subsequently ruled out using electron beam ion trap (EBIT) experiments (Bulbul et al. 2019; Gall et al. 2019; Weller et al. 2019). A current leading interpretation is charge exchange (CX) between bare Sulfur ions and neutral Hydrogen, described by Bulbul et al. (2014a), Gu et al. (2015), Shah et al. (2016), and others referenced therein. These explanations, and all others that feature baryonic matter, can be tested by considering the flux of the 3.5 keV line as a function of distance from the Galactic Center. This can then be compared to the predictions made for decaying dark matter by the Navarro-Frenk-White (NFW) profile (Navarro et al. 1997). The degree to which the flux profile matches the NFW profile represents the likelihood that the 3.5 keV line arises from decaying dark matter, since baryonic matter has a different distribution function. Recently, Boyarsky et al. (2018) showed rough consistency between the 3.5 keV line flux profile and the NFW profile in the region between 10 arcmin and 35 deg from the Galactic Center.

In this work, we employ a methodology designed to reach the most decisive conclusions on the 3.5 keV line to date. We utilize an extremely comprehensive data set in which we minimize signals from baryonic matter by restricting our search to the Milky Way's Dark Matter Halo. Furthermore, we use data from *Chandra* due to its high angular resolution and stable particle background relative to *XMM-Newton*. These features specific to *Chandra* give us the ability to detect a faint feature such as the putative 3.5 keV line. The results yielded by this ideal data set will then allow us to thoroughly explore the possibility of the 3.5 keV line's decaying dark matter interpretation.

2. DATA SELECTION

This work considers the entirety of archival *Chandra* observations that peer through the Milky Way's Dark Matter Halo and were documented by the *Chandra* Source Catalog Release 2.0 (CSC 2.0; Evans et al. 2010; Evans et al. 2019) as of July 2019. This includes

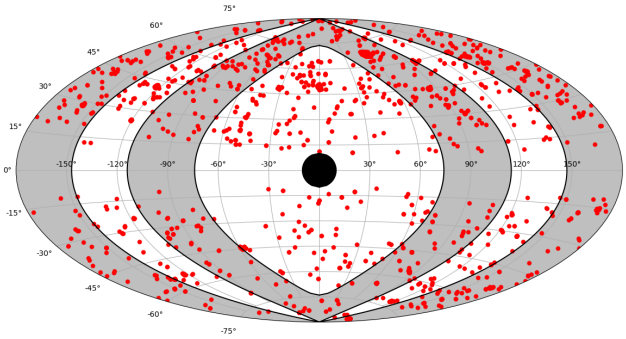


Figure 1. The positions of all 1907 observations used in the final data set, plotted in galactic coordinates. The black region represents the excluded Galactic Center (up to an angular distance of 10 deg), while the alternating white and gray regions represent the 4 regions of varying angular distance. Note that no observations appear between $b = -10$ deg and $b = 10$ deg due to the exclusion of the Galactic Disc.

observations from 2000–2014, compared to the CSC 1.1, which includes data only up to 2009. The initial data set contains ∼94 Ms of exposure time. The final data set (after performing the cleaning process described below) consists of 1907 observations and contains ∼51 Ms, making this the most rigorous search for the 3.5 keV line to date and the largest data set in the history of X-ray astronomy. Notably, the data set (originally ∼94 Ms, ∼51 Ms when cleaned) is larger than that of the similar study of archival *XMM-Newton* data by Dessert et al. (2020) (originally ∼86 Ms, ∼31 Ms when cleaned). Furthermore, *Chandra* is better-suited for this analysis than *XMM-Newton*. This is due in part to its ability to resolve as much as ∼80% of the Cosmic X-Ray Background (CXB; Hickox & Markevitch 2007), thus serving to isolate any possible signal from decaying dark matter. Moreover, *Chandra*'s particle background is substantially more stable than that of *XMM-Newton*, which varies by up to a factor of ∼10 on small scales due to solar flares (Bulbul et al. 2020), thus making *Chandra* more sensitive to weak line searches when considering large data sets.

We consider only observations performed in `VFAINT` mode by front-illuminated (FI) CCDs of the Advanced CCD Imaging Spectrometer (ACIS; Garmire et al. 2003), due to the well-known continuum behavior of the front-illuminated ACIS particle background (see Hickox & Markevitch 2006 and Bartalucci et al. 2014). This includes all of ACIS-I (CCD IDs 0, 1, 2, and 3) and ACIS-S2 (CCD ID 6). To avoid contamination from the Galactic Center or Galactic Disc, we used only observations at latitudes $|b| \geq 10$ deg. In addition, we restricted our data to observations with $N_H < 10^{22}$ cm^{-2} to mini-

Bin	θ_{GC} [deg]	t_{exp} [Ms]	ObsIDs	Counts (w/sources)	Counts (w/out)	A_i [deg^2]	A_f [deg^2]
1	10–74	8.00	306	1569344	1224559	19.18	13.44
2	74–114	14.07	715	3540528	2666281	57.96	43.98
3	114–147	17.58	473	4374038	2785435	36.24	19.57
4	>147	11.00	413	2466970	1855048	27.63	19.05
	TOTAL	50.65	1907	11950880	8531323	141.01	96.04

Table 1. Breakdown of the angular distance bins showing the distances and amount of data contained in each, with the latter expressed in terms of exposure time (t_{exp}), number of observations (ObsIDs), and number of photons (counts) both before and after source removal. A_i and A_f denote the total detector exposure area before and after source removal, respectively. Note that the counts given here reflect the 2.9–5.6 keV energy band on which we analyze all spectra.

mize the presence of ubiquitous baryonic matter. Upon compiling the list of observations compliant with these criteria, we downloaded those observations directly from the *Chandra* archive. The only Galactic contamination remaining in the final data set is the unavoidable Hot Gas Halo, but its contribution to the X-ray spectrum is notable only in bands much softer than 3.5 keV (Kuntz & Snowden 2000a; Kuntz & Snowden 2000b), which is therefore inconsequential to our analysis.

Making use of X-ray source detections reported in the CSC, all the point-sources in the selected fields were excised. In particular, the CSC 2.0 detects sources in stacks of observations, meaning that not all sources in a given observation's field of view (FOV) will necessarily contribute to the data collected by that observation. Our treatment, then, is extremely conservative, leaving virtually no contribution from point-sources in the final data set. To prevent contamination from extended emission, we removed all observations belonging to stacks containing extended sources. This was accomplished by first searching the list of extended sources reported in the CSC and removing all observations in stacks with extended emission, then by screening the target names of all remaining observations for low surface brightness extended sources missed by the CSC and removing all observations in the corresponding stacks. We then eliminated all observations containing any instances of instrumental temperature beyond the nominal ACIS operating range, in particular above 159 K. Lastly, after reducing the data, observations with insufficient statistics were removed. After all data reduction and removal of unsatisfactory observations, we are left with the final ∼51 Ms data set. The spatial distribution of our final 1907 observations can be seen in Figure 1.

For the background, ACIS stowed data was utilized instead of the typical blank sky files. This was done for the purpose of considering the detector particle background and the unresolved CXB separately. The blank sky files are not suitable for this analysis due to their intrinsic inclusion of the Dark Matter Halo.

3. DATA REDUCTION

The data reduction was performed using *Chandra* Interactive Analysis of Observations (CIAO; Fruscione et al. 2006). First, raw data was calibrated according to the *Chandra* Calibration Database (CALDB) version 4.8.3 using the CIAO tool `chandra_repro`, ensuring the preservation of `VFAINT` data using `check_vf_pha=yes`. Each observation was then matched with a background event file. The background file was produced using the CIAO tool `dmmerge` to combine the proper ACIS stowed files. These stowed files were identified using two criteria, namely epoch and active CCD numbers. The epoch was determined using the `DATE-OBS` value in the header of the observation's event file, and the active CCD numbers were determined using the `DETNAM` value in the header. All stowed files from the same epoch and from any CCD active in the observation were merged to produce the final background file. This ensured proper compatibility of the particle background with all observations, including matching calibration.

Light-curve filtering was applied to the data to remove background flares. This produced good time interval (GTI) files used to create cleaned event files. The stowed file for each observation was reprojected to match the coordinates of the observation.

The CSC was then used to remove all point-sources in each observation. After following the highly conservative protocol described in section 2 to identify the point-sources, the point spread function (PSF) width for each source, given in the CSC at 1σ confidence, was utilized to establish the effective extension of the point-source in the data. To be conservative, we used the corresponding 5σ PSF width. For the numerous sources given in the CSC, but not supplied with PSF widths, we used a width corresponding to a circle of radius 5" to maximize removal of contamination while preserving our data. A region file containing all sources for each observation was made using this data together with the CIAO tool `dmmakereg`. This region was then inverted, resulting in

a region file containing no sources, which was subsequently used as a spatial filter, on both the observation and the background, in the spectral extraction process.

After applying the spatial filter to each stowed file, and hence removing regions corresponding to sources in its associated observation, the exposure time of the stowed file was rescaled to match that of the observation. It should be noted that all observations in the data set had exposure times smaller than 200 ks, while all background exposure times are greater than 240 ks, and therefore there is no case in which the background exposure time was artificially increased. This was done to properly match each observation's particle background spectrum (also referred to as "stowed spectrum" or "background spectrum" hereafter) with the data, allowing us to properly weight each contributing background spectrum in the stacked background spectra. Here, "weight" refers to the influence the spectrum from a particular CCD in a particular ACIS stowed observation has on the final stacked spectrum, which must be based on both its exposure time in observations from that epoch and on the particle background flux at the exact time of the corresponding observations. Our methodology achieves correct weighting by, through the stacking process, inherently scaling the contribution of each particular CCD's stowed spectrum from the ACIS stowed observations to that CCD's same contribution to the data set, resulting in a stacked stowed spectrum displaying the same behavior as the particle background component of the data set's stacked spectrum.

Note that simply stacking the 3 original stowed files without first matching and rescaling them for each observation (to give 1907 tailored stowed spectra) produces a spectrum incompatible with the particle background contributions to the data set's stacked spectrum, since stacking the original stowed files would inherently and erroneously give equal weights to the stowed spectra of all CCDs used in the analysis and hence produce an incorrectly-shaped particle background spectrum. In contrast, as stated above, our method implicitly assigns the correct weight to each CCD, resulting in a particle background spectrum consistent with the data set. Also note that assigning weights based only on exposure time is similarly insufficient, since it fails to consider the variable particle background flux, while our method inherently accounts for all necessary factors to successfully produce a particle background spectrum correctly-matched to the data set.

The spectrum, redistribution matrix file (RMF), and ancillary response file (ARF) of each observation were obtained using the CIAO tool `specextract`, and the corresponding stowed spectrum was obtained using `dmextract`. No ARFs were obtained for the stowed data due to none of its signal passing through *Chandra*'s High Resolution Mirror Assembly (HRMA), but RMFs were generated using methods similar to those employed by Hickox & Markevitch (2006) and Bartalucci et al. (2014).

Finally, the counts of each stowed spectrum were rescaled to match the corresponding observation using 2 principles of the ACIS particle background spectrum, both of which are detailed in Hickox & Markevitch (2006). First, the shape of the spectrum is known to stay constant (within ∼1–2%), while the flux varies with the spacecraft's position. And second, *Chandra*'s effective area is very low in the 9.5–12 keV band, and hence the particle background dominates. Exploiting these principles to normalize each stowed spectrum, we thus obtained a final corresponding particle background spectrum for each spectrum in the data set. Upon extracting and normalizing all spectra, `combine_spectra` was used to merge them into a total of five stacked spectra to use in the analysis.

First, the spectra from all 1907 observations were stacked to produce one spectrum containing the entirety of the data set. All stowed spectra were stacked to produce the corresponding particle background spectrum.

The other four stacked spectra represent our four bins of angular distance from the Galactic Center, which can be used to study the possible decaying dark matter origins of the 3.5 keV line. The size of each bin is unique and was determined with the goal of producing as many bins as possible that contain sufficient exposure time for making a 3σ detection of the 3.5 keV line, calculated based on the 3σ detection made using *Chandra* by Cappelluti et al. (2018) and assuming an NFW profile for the line intensity.

To produce the bins, we computed each observation's distance from the Galactic Center based on its pointing coordinates. This distance was used to place it in one of the angular distance bins, according to our aforementioned criteria, resulting in 4 bins of angular distances, detailed in Table 1. Henceforth, the bins will be referred to as bins 1, 2, 3, and 4, numerically ordered by increasing angular distance from the Galactic Center.

Upon obtaining the five final spectra, the corresponding stowed spectra were also stacked to match them. Finally, the exposure time of each stacked stowed spectrum was readjusted from the data set's exposure time (a relic of our weighting method) to its actual value of 1022352.6 s (see Table 2) to ensure correct statistics, with counts scaled accordingly to preserve proper normalization of

the count rate. These particle background spectra can be seen in Figure 14, found in the Appendix.[1]

4. ANALYSIS

The data analysis was performed using the spectral fitting package XSPEC 12.10.1f (Arnaud 1996) via the PyXspec 2.0.3 interface (Arnaud 2016). All spectra were modeled using two approaches. The first involves subtracting the particle background before modeling and the second incorporates a particle background model ("background-subtracted" and "background-modeled" henceforth, respectively). Gaussian statistics are used throughout due to the sufficient counts contained by all energy bins (Protassov et al. 2002). All background-subtracted spectra are binned such that each bin contains a minimum of 30 counts, while all background-modeled spectra are unbinned (including those analyzed in section 4.4).

4.1. *Treatment of the Background*

As previously mentioned, this analysis requires ACIS stowed spectra rather than blank sky spectra to avoid including a dark matter signal in the background. The ACIS stowed data contains only particle background, so the unresolved CXB was modeled separately.

A pivotal feature of the particle background is its low statistics relative to the data set. In 20 years of *Chandra*, only ∼1 Ms of stowed observations has been taken (detailed in Table 2). However, our data set contains ∼51 Ms, putting its high count statistics at risk of inheriting noise from the relatively low particle background exposure. This effect is amplified by the prevalence of *Chandra*'s particle background flux above ∼2 keV, which is especially dominant in observations after source-removal. In Table 3, we illustrate this using the signal-to-noise ratio in the data set before and after source removal on the band used in our analysis.

The low particle background statistics substantially hinders the background-subtracted results, making the background-modeled method far more statistically robust. However, the simplicity of the background-subtracted models is a possible advantage over the highly more complex background-modeled models, hence providing motivation to include background-subtraction in the analysis. Moreover, it can be useful when placed in the context of similar works, particularly Cappelluti et al. (2018).

Year	t_{exp} [Ms]
2000	0.415
2005	0.367
2009	0.240
TOTAL	1.022

Table 2. Total exposure time of the three *Chandra* ACIS stowed observations.

[1] Note that Figures 14 and beyond (up to the final Figure 27) are located in the Appendix.

Data	Total Counts	Particle Background Counts	Signal-to-Noise
Full fields	151177565	139226685	971.98
Source-removed	126560247	118028924	758.35

Table 3. Signal-to-noise ratio before and after excising sources. Counts are calculated on the 2.9–5.6 keV band analyzed in our models. Particle background counts are estimated using the rescaled and renormalized ∼1 Ms ACIS stowed data.

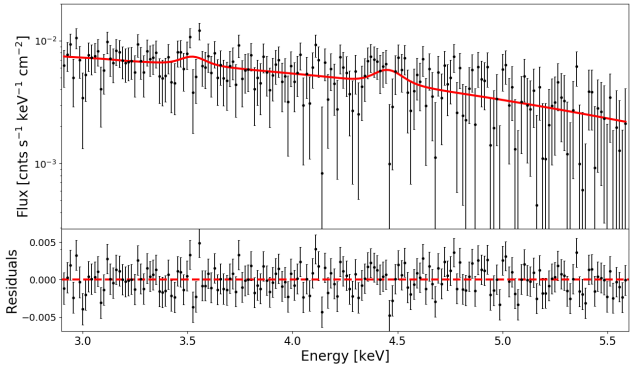


Figure 2. Background-subtracted spectrum stacked from all observations in the data set.

4.2. *Background-Subtracted Modeling*

Each spectrum was modeled in the 2.9–5.6 keV band, chosen to be wide enough for establishing a reliable power-law component while minimizing total free parameters by avoiding emission features. The unresolved CXB continuum was modeled using an absorbed (`phabs` in XSPEC) power-law, with N_H fixed at 10^{20} cm^{-2}. This value is an approximation of the average column density across all fields used in the analysis, based on Dickey & Lockman (1990), and does not contribute to the band of interest. An emission line was fitted at ∼4.5 keV, in agreement with Cappelluti et al. (2018)'s detection of a similar feature. As described by Cappelluti et al. (2018), this feature is consistent with known instrumental lines due to Ti $K_{\alpha_{1,2}}$ at 4.51 keV and 4.50 keV, respectively, within *Chandra*'s energy resolution and the 1σ error range of our best-fit line energy values. The line is hard to detect in the ∼1 Ms of ACIS stowed data, but

Parameter [Unit]	All	Bin 1	Bin 2	Bin 3	Bin 4
Γ_{PL}	$1.42^{+0.18}_{-0.18}$	$1.38^{+0.16}_{-0.16}$	$1.51^{+0.19}_{-0.19}$	$1.35^{+0.2}_{-0.2}$	$1.45^{+0.18}_{-0.18}$
I_{PL} [10^{-4} ph s^{-1} cm^{-2}]	$1.26^{+0.33}_{-0.27}$	$1.35^{+0.33}_{-0.26}$	$1.45^{+0.4}_{-0.32}$	$1.02^{+0.31}_{-0.24}$	$1.38^{+0.38}_{-0.3}$
$E_{4.5}$ [keV]	$4.46^{+0.08}_{-0.04}$	$4.46^{+0.07}_{-0.04}$	$4.47^{+0.08}_{-0.05}$	$4.46^{+0.08}_{-0.04}$	$4.46^{+0.08}_{-0.04}$
$I_{4.5}$ [10^{-7} ph s^{-1} cm^{-2}]	$8.37^{+4.82}_{-4.39}$	$9.06^{+4.97}_{-4.75}$	$8.24^{+5.02}_{-4.6}$	$8.53^{+4.62}_{-4.4}$	$9.04^{+4.98}_{-4.72}$

Table 4. Best-fit model parameters for all background-subtracted spectra with 1σ errors.

appears more clearly in the ∼10 Ms of data in Cappelluti et al. (2018) and the ∼51 Ms in this work due to the considerably higher statistics of the data sets.

To probe the possibility of a 3.5 keV feature in our data, we added an additional Gaussian emission line component at ∼3.5 keV in all spectra, with the energy left free to vary between 3.4–3.6 keV. The best-fit energy and flux of the line in each spectrum is reported in Table 5, with values of $3.53^{+0.04}_{-0.05}$ keV and $6.03^{+4.3}_{-3.69}$ 10^{-7} ph s^{-1} cm^{-2}, respectively, in the spectrum stacked from the total data set. Each spectrum is plotted with the line (Figures 2 and 15). All parameters were left free to vary, apart from the fixed N_H and widths of emission lines, which were frozen at 0 keV and hence dictated by *Chandra*'s energy resolution after being folded through the response files. This left a total of 6 free parameters, including those describing the 3.5 keV line component. Best-fit parameters for the power-law and ∼4.5 keV feature are reported in Table 4.

All best-fit values were obtained using the Markov-Chain Monte-Carlo (MCMC) in XSPEC. An MCMC was performed for each spectrum, using the Metropolis-Hastings (MH) algorithm and random priors, employing the χ^2 fit statistic on the binned data. Each chain consisted of 1,000,000 runs after discarding the first 40,000 to constitute a burn-in period. For each parameter, the best-fit value is the 0.5 quantile of its MCMC distribution, and 1σ lower and upper errors are the 0.16 and 0.84 quantiles, respectively. These values reflect the Gaussian mean for the best-fit, and the Gaussian standard deviation for the 1σ errors. The results of the MCMC analysis for each spectrum are given in Figures 16, and 17 with confidence contours plotted at 1, 2, and 3σ according to the 2-dimensional Gaussian distribution.

Bin	$E_{3.5}$ [keV]	$I_{3.5}$ [10^{-7} ph s^{-1} cm^{-2}]
1	$3.52^{+0.04}_{-0.06}$	$5.16^{+4.35}_{-3.35}$
2	$3.53^{+0.04}_{-0.06}$	$5.58^{+4.46}_{-3.62}$
3	$3.53^{+0.03}_{-0.03}$	$8.39^{+4.36}_{-4.28}$
4	$3.52^{+0.05}_{-0.06}$	$4.73^{+4.12}_{-3.14}$
ALL	$3.53^{+0.04}_{-0.05}$	$6.03^{+4.30}_{-3.69}$

Table 5. Best-fit 3.5 keV line energy and normalization for each background-subtracted spectrum with 1σ errors.

Due to the background-dominated nature of *Chandra* observations, especially in our source-removed data, the MCMC analysis was crucial. High background counts are well-known to cause difficulty in detecting faint emission lines, so the statistically powerful MCMC was employed to combat these statistical issues, since its large volume of runs and Bayesian approach are well-suited for a faint feature such as the putative 3.5 keV line. The ∼3.5 keV line energy MCMC probability distribution shows Gaussian convergence to the best-fit values, suggesting the possible presence of a feature.

4.2.1. *Chi-Squared Testing*

All χ^2 testing results are reported in Table 6. The reduced χ^2 of all models was between ∼0.80 and ∼0.90, both with and without the ∼3.5 keV feature, suggesting the models fit the data very well. The significance of the ∼3.5 keV feature is low, at only 1.08σ in the total data set, estimated via the $\Delta\chi^2$ method. Bin 3, which includes the region where Cappelluti et al. (2018) made a possible detection, shows the highest significance of all spectra but is consistent only with a 1.72σ statistical fluctuation. Hence, the χ^2 analysis suggests a non-detection in the total data set and in all bins.

4.2.2. *Bayesian Information Criterion*

The Bayesian Information Criterion (BIC; Schwarz 1978; Wit et al. 2012) is a powerful tool for evaluating and comparing models. A lower BIC is favorable (Kass & Raftery 1995), and the difference (ΔBIC) between two models can be used to estimate the significance of a feature in a nested model such as ours. Thus, to ensure a robust and composite statistical treatment, we employed the BIC in addition to our χ^2 analysis, the results of which are reported in Table 7. The significance of the line yielded by the BIC analysis is substantially lower than that of $\Delta\chi^2$ in all spectra, at only 0.02σ in the total data set and only 0.06σ in bin 3. This firmly supports the claim that the apparent feature is a statistical fluctuation and allows us to conclude a non-detection for the background-subtracted results.

4.2.3. *Peculiarities in ACIS Stowed Spectra*

An important step of performing background subtraction was examining the particle background spectra

for artifacts that could result in a spurious feature in our analysis and others that utilize ACIS stowed data. There appears to be an artifact around 3.5 keV in some of the stowed spectra (shown in Figures 18, 19, and 20). In particular, there appear to be anomalously scattered points below the continuum in various such spectra.

Thorough checks were performed on the background data, and it was found that the spurious points appear in both the PHA and PI spectra, even when filtering for only good event grades (0, 2, 3, 4, and 6). Moreover, the feature appears prominently when all stowed spectra are stacked to form the data set's particle background spectra, and hence was modeled as a Gaussian absorption line in each stacked background spectrum (Figures 3 and 21).

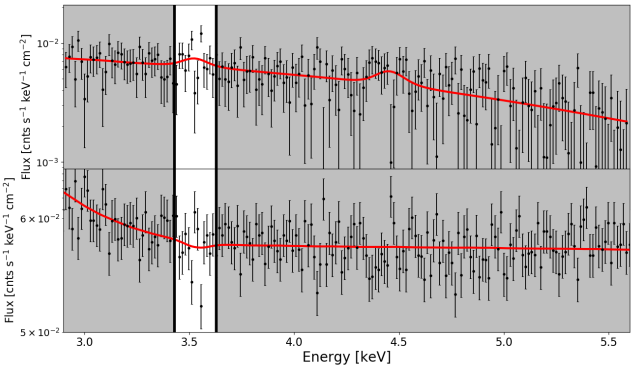


Figure 3. Background-subtracted spectrum of the entire data set modeled with a 3.5 keV line (top), compared to the corresponding background spectrum containing the 3.5 keV dip (bottom).

The data model's emission feature and the background model's dip occur within the same error range of energy, suggesting that subtracting the background's dip could cause the false appearance of emission feature. In fact, the two highest data points above the continuum in the modeled emission line occur at the exact energies as the most spuriously low data points in the particle background dip, leading to the conclusion that even our statistically insignificant modeled feature here is impacted by this background artifact.

The dip does not follow a Gaussian absorption profile, as it is defined only by the two anomalous data points above an otherwise smooth continuum. Furthermore, the energies of the two points are in close proximity, rivaling the spectral resolution of *Chandra*. Hence, after being folded through the RMF and thus accounting for the *Chandra* energy resolution, a Gaussian dip cannot properly fit the data. Indeed, as seen in Figure 3, the modeled feature does not properly account for the peculiarity, considerably underestimating the depth of the dip. This results in the dip model component having a negligible statistical significance. Due to *Chandra*'s energy resolution, the Gaussian absorption line will always be too wide to fit a sharp spike consisting of only two nearby data points. Regardless, the spurious points will inevitably exaggerate any possible feature at ∼3.5 keV in a background-subtracted spectrum, casting doubt on any possible detection.

In this case, the background artifact has clearly amplified the 3.5 keV feature, though with the low significance estimates yielded by both the χ^2 and BIC analyses, it is nonetheless clear that any such feature is consistent only with a statistical fluctuation. It is unclear, however, what role these spurious particle background points may have played in previous works, including the possible Cappelluti et al. (2018) detection.

Due to the unknown extent of the spurious artifact's influence on the data, in addition to the lowered statistics after subtracting the background, we do not consider the results of the background-subtracted analysis definitive. We conclude that the background-modeled analysis is needed to properly utilize our ∼51 Ms data set, and hence opt to treat the background-subtracted results as a preliminary test of the data. Modeling the background overcomes the low exposure of ACIS stowed data, yielding a high-statistics continuum free from the influence of statistical fluctuations, including the spurious dip data points, as such fluctuations are mitigated by our ∼51 Ms of exposure time. Moreover, the particle background normalization method employed here introduces a ∼2% systematic uncertainty in the background-subtracted continuum (Hickox & Markevitch 2006). This, too, is avoided in the background-modeled procedure, which yields a model accounting for all spectral components observed in the ∼51 Ms of data, including the particle background. The resulting model's continuum, then, is a model of the true continuum, and hence the systematic uncertainty becomes negligible, contributing only to the particle background component's priors. The conclusions reached by this work, and the computation of upper-limits in the case of a non-detection, will thus be predicated upon the statistically superior background-modeled results.

4.3. *Background-Modeled Modeling*

Each spectrum was analyzed on the 2.9–5.6 keV band, where models produced highly reliable fits, to maintain consistency with the band analyzed in the background-subtracted procedure. It was necessary to initially include the 1.9–2.9 keV band in the models to achieve good fits between 2.9 keV to ∼3.3 keV due to the contribu-

Bin	χ^2 w/line (DOF=178)	χ^2 w/out (DOF=180)	$\Delta\chi^2$ (ΔDOF=2)	Detection Probability	Line Significance
1	156.56	158.10	1.54	0.538	0.74σ
2	147.94	149.49	1.55	0.539	0.74σ
3	158.62	163.54	4.91	0.914	1.72σ
4	159.03	160.01	0.98	0.388	0.51σ
ALL	143.12	145.66	2.53	0.718	1.08σ

Table 6. The results of χ^2 testing on background-subtracted spectra. Note that DOF denotes degrees of freedom.

Bin	ΔBIC	Evidence **against** Model w/Line	Bayes Factor	Detection Probability	Line Significance
1	9.07	Strong	93.23	0.011	0.01σ
2	9.00	Strong	89.85	0.011	0.01σ
3	6.10	Strong	21.09	0.045	0.06σ
4	9.52	Strong	116.79	0.008	0.01σ
ALL	8.15	Strong	58.86	0.017	0.02σ

Table 7. The results of BIC testing on background-subtracted spectra. The strength of evidence against the model with a line at 3.51 keV is determined via the standard scale used to qualitatively interpret the ΔBIC and corresponding Bayes Factor, originally established by Kass & Raftery (1995).

tion of a known mother-daughter emission line system starting at ∼2 keV (Bartalucci et al. 2014).

The total model is the sum of a particle background model and an astrophysical model. The particle background model was folded through its RMF, while the astrophysical model was folded through the data's RMF and ARF, with the latter accounting for the photons' passage through *Chandra*'s HRMA.

Best-fit parameters for each model were obtained, again, via MCMC in XSPEC. However, while the background-subtracted procedure utilized the MH algorithm due to its ability to set random priors, the background-modeled method employs the Goodman-Weare (GW) algorithm. Unlike MH, GW's priors are obtained from the covariance matrix of a preliminary C-statistic (CSTAT; Cash 1979) fit. It also operates via any number of random walkers that can be run in parallel, greatly decreasing computing costs. These features are highly advantageous to the large and degenerate nature of the background-modeled parameter space, allowing the chain to use reliable priors and perform a large volume of runs on substantially shorter time scales than MH. The chain for each model consisted of 2,700,000 runs, with 30 walkers and a burn-in period of 216,000, offering highly robust statistics to the modeling process. The algorithm employed the CSTAT

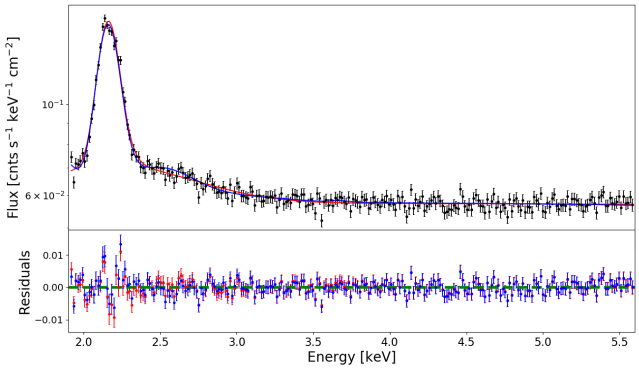


Figure 4. Two models of the particle background plotted against the ∼1 Ms of ACIS stowed data. **Red**: The simpler model with 2 Gaussian components. **Blue**: The more complex model necessary for our background-modeled analysis containing 4 Gaussian components, in addition to the 3.3 keV and 3.68 keV emission features.

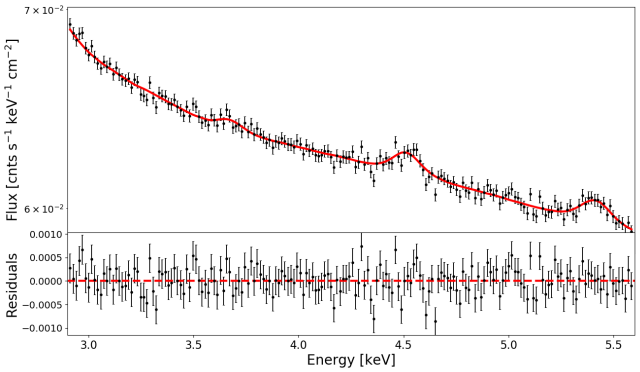


Figure 5. Background-modeled spectrum stacked from all observations in the data set.

Parameter [Unit]	All	Bin 1	Bin 2	Bin 3	Bin 4
Γ_{PL}	$1.41^{+0.13}_{-0.08}$	$1.46^{+0.03}_{-0.01}$	$1.5^{+0.08}_{-0.08}$	$1.42^{+0.26}_{-0.1}$	$1.33^{+0.07}_{-0.07}$
I_{PL} [10^{-4} ph s^{-1} cm^{-2}]	$1.25^{+0.18}_{-0.11}$	$1.46^{+0.05}_{-0.03}$	$1.42^{+0.13}_{-0.12}$	$1.13^{+0.36}_{-0.12}$	$1.19^{+0.11}_{-0.1}$
Γ_{PBK}	$11.34^{+0.48}_{-0.53}$	$12.96^{+0.04}_{-0.04}$	$10.1^{+0.75}_{-0.71}$	$12.13^{+0.58}_{-0.57}$	$11.66^{+0.81}_{-0.96}$
I_{PBK} [ph s^{-1} cm^{-2}]	$12.0^{+1.76}_{-2.06}$	$11.27^{+0.09}_{-0.07}$	$6.95^{+2.71}_{-2.09}$	$14.09^{+3.06}_{-4.75}$	$12.23^{+3.58}_{-3.92}$
$E_{4.5}$ [keV]	$4.51^{+0.01}_{-0.01}$	$4.5^{+0.02}_{-0.02}$	$4.53^{+0.02}_{-0.02}$	$4.51^{+0.02}_{-0.02}$	$4.5^{+0.03}_{-0.03}$
$I_{4.5}$ [10^{-7} ph s^{-1} cm^{-2}]	$6.22^{+0.79}_{-0.79}$	$6.28^{+1.91}_{-0.96}$	$6.77^{+1.7}_{-1.74}$	$7.34^{+1.05}_{-1.24}$	$5.24^{+1.83}_{-1.61}$
$E_{5.4}$ [keV]	$5.41^{+0.01}_{-0.01}$	$5.41^{+0.02}_{-0.01}$	$5.42^{+0.01}_{-0.01}$	$5.43^{+0.01}_{-0.02}$	$5.4^{+0.01}_{-0.01}$
$I_{5.4}$ [10^{-7} ph s^{-1} cm^{-2}]	$9.92^{+1.36}_{-1.15}$	$9.57^{+1.16}_{-1.16}$	$12.86^{+2.67}_{-2.55}$	$9.46^{+1.49}_{-1.06}$	$9.45^{+1.83}_{-1.04}$
E_1 [keV]	$2.78^{+0.09}_{-0.09}$	$2.74^{+0.13}_{-0.13}$	$2.63^{+0.13}_{-0.12}$	$2.67^{+0.16}_{-0.15}$	$2.63^{+0.19}_{-0.19}$
σ_1 [keV]	$0.42^{+0.05}_{-0.05}$	$0.44^{+0.1}_{-0.05}$	$0.41^{+0.09}_{-0.07}$	$0.49^{+0.01}_{-0.05}$	$0.5^{+0.09}_{-0.08}$
I_1 [10^{-2} ph s^{-1} cm^{-2}]	$0.33^{+0.09}_{-0.07}$	$0.38^{+0.11}_{-0.12}$	$0.47^{+0.16}_{-0.14}$	$0.42^{+0.14}_{-0.11}$	$0.56^{+0.24}_{-0.19}$
E_2 [keV]	$2.16^{+0.0}_{-0.0}$	$2.16^{+0.0}_{-0.0}$	$2.16^{+0.0}_{-0.0}$	$2.16^{+0.0}_{-0.0}$	$2.16^{+0.0}_{-0.0}$
σ_2 [10^{-2} keV]	$5.02^{+0.04}_{-0.04}$	$4.94^{+0.06}_{-0.08}$	$4.96^{+0.06}_{-0.06}$	$5.06^{+0.07}_{-0.07}$	$5.03^{+0.08}_{-0.08}$
I_2 [10^{-2} ph s^{-1} cm^{-2}]	$1.87^{+0.01}_{-0.01}$	$1.78^{+0.01}_{-0.02}$	$2.07^{+0.02}_{-0.02}$	$1.73^{+0.02}_{-0.02}$	$1.89^{+0.03}_{-0.03}$
E_3 [keV]	$2.5^{+0.0}_{-0.0}$	$2.49^{+0.01}_{-0.01}$	$2.51^{+0.01}_{-0.01}$	$2.51^{+0.01}_{-0.01}$	$2.5^{+0.01}_{-0.01}$
σ_3 [keV]	$0.19^{+0.01}_{-0.01}$	$0.2^{+0.02}_{-0.02}$	$0.17^{+0.01}_{-0.01}$	$0.18^{+0.02}_{-0.02}$	$0.19^{+0.02}_{-0.02}$
I_3 [10^{-2} ph s^{-1} cm^{-2}]	$0.5^{+0.05}_{-0.05}$	$0.52^{+0.09}_{-0.12}$	$0.42^{+0.08}_{-0.07}$	$0.42^{+0.08}_{-0.08}$	$0.48^{+0.1}_{-0.09}$
E_4 [keV]	$2.87^{+0.29}_{-0.26}$	$3.04^{+0.25}_{-0.36}$	$2.85^{+0.29}_{-0.25}$	$3.0^{+0.25}_{-0.34}$	$2.98^{+0.23}_{-0.31}$
σ_4 [keV]	$13.39^{+1.61}_{-1.43}$	$14.9^{+3.33}_{-3.94}$	$12.09^{+1.68}_{-1.26}$	$15.37^{+2.97}_{-3.57}$	$15.61^{+2.59}_{-2.32}$
I_4 [ph s^{-1} cm^{-2}]	$1.95^{+0.23}_{-0.2}$	$2.06^{+0.45}_{-0.54}$	$1.95^{+0.26}_{-0.2}$	$2.06^{+0.39}_{-0.47}$	$2.32^{+0.38}_{-0.34}$
$I_{3.7}$ [10^{-5} ph s^{-1} cm^{-2}]	$7.5^{+2.85}_{-3.12}$	$7.11^{+2.85}_{-4.09}$	$7.31^{+4.07}_{-3.54}$	$8.34^{+3.9}_{-2.86}$	$10.65^{+4.15}_{-4.43}$
$I_{3.3}$ [10^{-5} ph s^{-1} cm^{-2}]	$0.97^{+1.33}_{-0.72}$	$0.06^{+1.11}_{-0.01}$	$2.0^{+2.92}_{-1.46}$	$0.0^{+0.5}_{-0.0}$	$6.45^{+2.87}_{-2.18}$

Table 8. Best-fit model parameters for the background-modeled spectra with 1σ errors. The astrophysical parameters are reported in the upper panel, while particle background parameters are reported in the lower panel.

fit statistic in favor of χ^2 to properly accommodate the unbinned data. Best-fit values and 1σ errors were again computed to correspond to the Gaussian means and standard deviations of the resulting parameter value distributions, respectively, using the same procedure described in section 4.2.

4.3.1. *Particle Background Model*

The particle background model consists of a power-law, in addition to Gaussian components to fit various emission features. This includes all observed effects of the mother-daughter system described by Bartalucci et al. (2014) as an artifact resulting from corrections for Charge Transfer Inefficiency (CTI, described extensively by Grant et al. 2005). Emission lines belonging to this system are the only lines in our models with non-zero and free-to-vary widths. All others have widths fixed at 0 keV before being folded through the relevant response files, thus dictating them according to instrumental energy resolution.

However, whereas Bartalucci et al. (2014) found a mother-daughter system containing two Gaussians, our analysis finds two additional Gaussians in the system. In particular, Bartalucci et al. (2014) models Gaussians at ∼2.16 keV and ∼2.26 keV, while our analysis includes Gaussians at 2.16 keV, 2.50 keV, 2.78 keV, and 2.87 keV, though these energies vary (apart from 2.16 keV) between models. Moreover, the widths of both Bartalucci et al. (2014) Gaussians are $\sim 10^{-1}$ keV while ours vary depending on the best-fit values obtained via our MCMC methodology. Moreover, Bartalucci et al. (2014) only observed the artifact from CTI correction to exist between 2–3 keV in the same ACIS stowed files used for this analysis, whereas it extends to ∼3.3 keV in our spectra. The mother-daughter feature is consistent with Bartalucci et al. (2014) in our lower-statistics

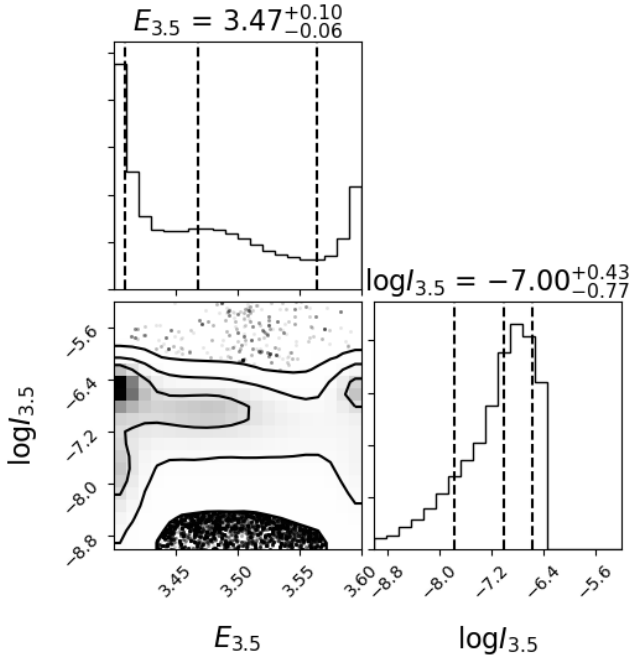


Figure 6. MCMC contour plot for 3.5 keV line parameters when energy is left free to vary between 3.4–3.6 keV.

spectra, namely our background spectra (Figure 14) and background-subtracted models (Figures 2 and 15).

The new extension of the CTI correction artifact only appears in our high-statistics background-modeled spectra (Figures 5 and 22). This suggests that the feature is simply difficult to distinguish from the continuum when dealing with spectra that do not contain the extremely high ∼51 Ms of data seen in our data set. Indeed, this is exemplified by Figure 4, where two models are able to fit the ∼1 Ms ACIS stowed spectrum. One model's CTI correction artifact is composed of the two Bartalucci et al. (2014) mother-daughter Gaussians, while the other is the model used in our background-modeled analysis, with four Gaussians. Both are plotted against the ∼1 Ms of stowed data in the figure, and the feature modeled in our ∼51 Ms spectrum can be seen blending with the continuum.

Two faint emission lines were modeled at 3.3 keV and 3.68 keV, with energies fixed at the known values also used in Abazajian (2020) and Boyarsky et al. (2020). These features are believed to arise from both astrophysical and instrumental emission lines, and hence to minimize our model's large parameter space we choose to treat the features as single emission lines (as in both Abazajian 2020 and Boyarsky et al. 2020) in the instrumental background model. The 3.3 keV line is thought to be a blend of Ar XVIII, S XVI, and K Kα, while the 3.68 keV line is thought to be due to Ar XVII or Ca Kα (Boyarsky et al. 2018; Abazajian 2020; Boyarsky et al. 2020).

The instrumental line seen in the background-subtracted spectra at ∼4.5 keV was again modeled here. An additional emission line was detected and fitted at ∼5.4 keV. This is another known instrumental line due to Cr Kα and has been seen in *Suzaku* (Sekiya et al. 2016) and *XMM-Newton* (Bulbul et al. 2020). Like the ∼4.5 keV line, it is not detectable in the ACIS stowed data due to the limited statistics, and unlike the ∼4.5 keV line it is difficult to resolve in the background-subtracted data. However, with the full statistics of our ∼51 Ms data set, it appears much more prominently.

In this analysis, the particle background model includes all particle background components with the exception of the ∼4.5 keV and ∼5.4 keV lines. These two components, though instrumental, are not detected in the ∼1 Ms of ACIS stowed data. In particular, the CSTAT fitting of a ∼4.5 keV emission line yields zero statistical significance, and the CSTAT fitting of a ∼5.4 keV emission line yields a small significance (∼1.4σ, as estimated by $\Delta\chi^2$) consistent only with a fluctuation. The lack of detection in the particle background spectrum of features that appear prominently in our stacked spectra thus prevents us from obtaining useful priors from the CSTAT fitting process and ultimately results in unreliable models with poor fits, even after running the MCMC procedure. To combat this, we included the ∼4.5 keV and ∼5.4 keV line components in the astrophysical model, which allowed us to properly account for their contributions.

4.3.2. *Astrophysical Model*

In addition to the ∼4.5 keV and ∼5.4 keV emission components, the astrophysical model contains the unresolved CXB continuum, again modeled using an absorbed power-law with N_H fixed at 10^{20} cm^{-2}, in addition to the possible 3.5 keV feature. The astrophysical and instrumental models thus combine for a total of 22 free parameters, before accounting for the addition of a 3.5 keV component.

4.3.3. *Modeling Without the 3.5 keV Line*

The spectra were initially modeled without the 3.5 keV feature, plotted in Figures 5 and 22 with best-fit parameters reported in Table 8. The models produced considerably good fits, with that of the total data set achieving a reduced χ^2 of exactly the ideal 1.00, with all models exhibiting reduced χ^2 values between 1.00 and 1.12.

A major result from these models is the flux and significance of the line at 3.68 keV, detected at 4.06σ in the total data set. This firmly refutes the Dessert et

al. (2020) fiducial model, which omits the 3.68 keV feature. Moreover, due to the thorough removal of baryonic material from our observations, particularly from the Galactic Disc, the prominence of the 3.68 keV line in our data suggests that it may be largely instrumental and hence likely due to Ca Kα emission.

The 3.68 keV line flux in our total data set is higher than in the Boyarsky et al. (2018) *XMM-Newton* analysis by a factor of ∼2. The Boyarsky et al. (2018) data set has smaller particle background statistics and hence yields a correspondingly smaller 3.68 keV line flux due to the large size of our data set. As observed via various other features in our particle background model, including the extension of the mother-daughter emission system and the 5.4 keV line, our robust particle background statistics reveal particle background features with previously unseen clarity. The prominence of the 3.68 keV line in our data, and its similar prominence in Boyarsky et al. (2018), further suggests it is largely instrumental. The consistency of this interpretation across works using both *Chandra* and *XMM-Newton*, namely this work and Boyarsky et al. (2018), suggests the instrumental emission at 3.68 keV is due to an effect common to both observatories, hence strengthening the refutation of the Dessert et al. (2020) analysis.

We also find a low flux and low significance for the 3.3 keV line in all models. This differs from Boyarsky et al. (2018), where the 3.3 keV line is found to have a higher flux than the 3.68 keV feature. The Boyarsky et al. (2018) data set also excises point-sources, but includes the Galactic Center and the Galactic Disc, yielding a higher density of baryonic matter. The contrasting low flux of the 3.3 keV feature in our data, then, suggests that it may be largely astrophysical.

4.3.4. *Free-to-vary 3.5 keV Line Energy*

To evaluate the possible presence of a feature at ∼3.5 keV, a Gaussian emission component was added to the model and the MCMC fitting procedure was repeated. Both the energy and normalization of the line were initially left free to vary, with energy again restricted to the interval 3.4–3.6 keV. Despite the statistical power offered by GW's CSTAT priors, it was critical to utilize random priors for the 3.5 keV component to avoid any bias from the CSTAT fitting process. Hence, for the free 3.5 keV line parameters, we employed a new method of generating Goodman-Weare priors in XSPEC.

We first performed our preliminary CSTAT fit to produce a set of initial priors for the method. Subsequently, we ran a Goodman-Weare MCMC chain with length 30 (one for each walker). The chain file was then edited, replacing the 3.5 keV energies and fluxes with appropriately randomized values, hence keeping all other initial priors while replacing the 3.5 keV component's priors with random values. The CSTAT values recorded in the chain of the 30 initial runs were adjusted to match the updated sets of parameters. Finally, a new chain was appended to this file with the properties mentioned above. This effectively offered random priors for the ∼3.5 keV line parameters, while still otherwise utilizing the advantages of GW's priors from CSTAT fitting. Also note that we evaluated a preliminary chain for correlations within the fit between the ∼3.5 keV line parameters and all other parameters, with the intention of randomizing any other parameters that showed high correlations (i.e., with Pearson Correlation Coefficient magnitudes greater than 0.8). None were found, and hence only the ∼3.5 keV line priors were randomized.

The parameter value distributions and contour plots for 3.5 keV line energy and normalization are shown in Figures 6 and 23, with confidence contours at 1, 2, and 3σ again in accordance with a 2-dimensional Gaussian distribution. The shape of the line energy distribution for the total data set indicates a non-detection, with the probability density reaching its minimum around 3.5 keV. Bins 1 and 4 exhibit this same behavior, while bins 2 and 3 have minor peaks near 3.5 keV. The probability density is highest around 3.5 keV, but in both cases, there appear to be other peaks near the edges of the parameter space, suggesting that any feature at 3.5 keV may not be significant.

We can thus reach preliminary conclusions that the 3.5 keV line was not detected in the total data set, nor was it detected in bins 1 and 4, and that there may be a feature in bins 2 and 3. We rigorously assess these hypotheses by fixing the line energy while leaving the line flux free to vary, thereby isolating the putative emission component. This can thus confirm non-detections and set upper-limits in the total data set, bin 1, and bin 4, while further evaluating the status of the possible feature in bins 2 and 3.

4.3.5. *Fixed 3.5 keV Line Energy*

The energy of the 3.5 keV emission component was fixed at 3.51 keV. This value was chosen to be consistent within the 1σ error ranges of various previous detections, including Boyarsky et al. (2014), Urban et al. (2015), and Cappelluti et al. (2018), and of the line energy probability distribution peaks in bins 2 and 3. Moreover, in a later section of this work (4.4), the same procedure used in section 4.3.4 was applied to our data set without point-source removal, and the line energy probability distribution in bin 3 was found to exhibit the sharpest central peak seen in the entirety of our

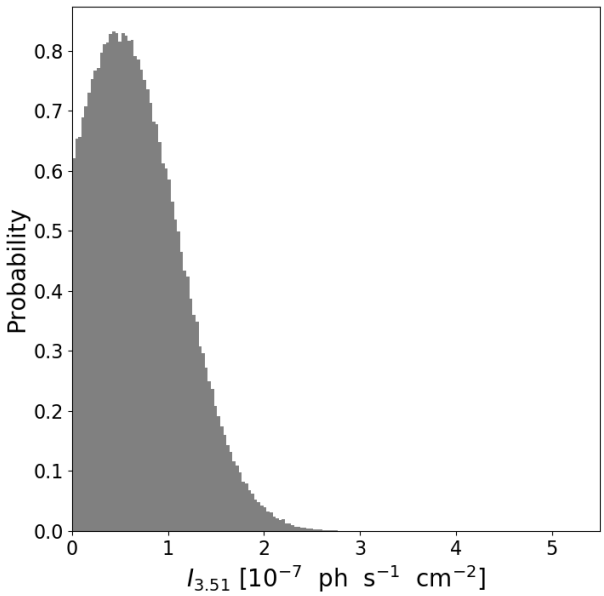


Figure 7. Probability density distribution for 3.51 keV line flux in the spectrum stacked from the total data set.

background-modeled analyses. This peak is found at 3.51 keV, hence solidifying our choice of line energy.

Running another MCMC chain with random priors for the line flux yields a probability density for each bin, shown in Figures 7 and 24, with the best-fit values and 1σ errors reported in Table 9. Using the best-fit value for the line flux in each model, we can evaluate the statistical significance of the possible feature in all spectra.

4.3.6. *Chi-Squared Testing*

The results of all χ^2 testing are reported in Table 10. The significance of the feature at 3.51 keV is low, estimated using the $\Delta\chi^2$ test at 0.72σ in the total data set. The feature exhibits zero statistical significance in both bin 1 and bin 4. In the bins with line energy probability density peaks at ∼3.5 keV, namely bins 2 and 3, the significance is estimated at only 0.74σ and 1.58σ, respectively, indicating that the possible feature is consistent only with a statistical fluctuation. Thus, the χ^2 analysis suggests a non-detection in the total data set and in all bins.

Bin	$I_{3.51}$ [10^{-7} ph s^{-1} cm^{-2}]
1	$0.83^{+1.02}_{-0.59}$
2	$1.30^{+1.06}_{-0.84}$
3	$1.66^{+0.95}_{-0.88}$
4	$0.57^{+0.75}_{-0.41}$
ALL	$0.65^{+0.53}_{-0.42}$

Table 9. Best-fit 3.51 keV line flux for each background-modeled spectrum with 1σ errors.

4.3.7. *BIC Testing*

The BIC testing results are reported in Table 11. The significance of the line is estimated by the ΔBIC test at 0.01σ in the total data set, a considerably smaller value than that yielded by $\Delta\chi^2$ testing. The feature, again, exhibits zero statistical significance in bins 1 and 4, and in this case has an estimated significance of only 0.01σ and 0.02σ in bins 2 and 3, respectively. In all cases of non-zero $\Delta\chi^2$ significance, ΔBIC yields substantially smaller estimates, strongly supporting the conclusion that any ∼3.5 keV feature in our data is consistent only with statistical fluctuations.

4.3.8. *Upper-Limits*

From these non-detections and the corresponding line flux probability distributions, we can set upper-limits on 3.5 keV line flux. To ensure the strength of the upper-limit for each spectrum, we compute the value using the 0.9985 quantile of the corresponding line flux probability distribution, representing the upper 3σ confidence interval[2]. The upper-limits are reported in Table 12 and will be used to constrain the sterile neutrino mixing angle and line flux radial profile.

4.4. *Data Without Point-Source Removal*

As shown earlier in Table 1, the point-source removal process greatly reduced the exposure area of our observations, which resulted in a less favorable signal-to-noise ratio (Table 3). To account for this and ensure point-source removal did not mask a ∼3.5 keV signal in our data, we thus applied our background-modeled procedure to the data set without removing point-sources, repeating the same methodology and utilizing the same models. Due to the higher exposure area, counts, and signal-to-noise ratio, these spectra offer a higher likelihood of detecting faint ∼3.5 keV emission from decaying dark matter in the Dark Matter Halo. If such a signal was detected in the models without source-removal, it would, of course, be difficult to disentangle from baryonic source emission within the scope of this work, and would require further study. However, non-detections would greatly reinforce the results of our analysis, and hence these source-intact models are highly valuable.

[2] Note that the correct upper 3σ quantile is 0.9985 and not 0.997. The lower 3σ quantile is 0.0015, which means a fraction 0.997 of the data correctly lies between the lower and upper 3σ quantiles.

Bin	χ^2 w/line (DOF=161)	χ^2 w/out (DOF=162)	$\Delta\chi^2$ (ΔDOF=1)	Detection Probability	Line Significance
1	182.17	181.35	-0.82	0.000	0.00σ
2	170.09	170.63	0.54	0.538	0.74σ
3	167.88	170.38	2.50	0.886	1.58σ
4	163.07	162.08	-1.00	0.000	0.00σ
ALL	161.38	161.90	0.52	0.529	0.72σ

Table 10. The results of χ^2 testing on background-modeled spectra. Note that DOF denotes degrees of freedom.

Bin	ΔBIC	Evidence **against** Model w/Line	Bayes Factor	Detection Probability	Line Significance
1	11.18	Very Strong	267.95	0.004	0.00σ
2	9.82	Strong	135.92	0.007	0.01σ
3	7.76	Strong	48.40	0.020	0.02σ
4	11.39	Very Strong	297.13	0.003	0.00σ
ALL	9.88	Strong	139.56	0.007	0.01σ

Table 11. The results of BIC testing on background-modeled spectra. The strength of evidence against the model with a line at 3.51 keV is determined via the standard scale used to qualitatively interpret the ΔBIC and corresponding Bayes Factor, originally established by Kass & Raftery (1995).

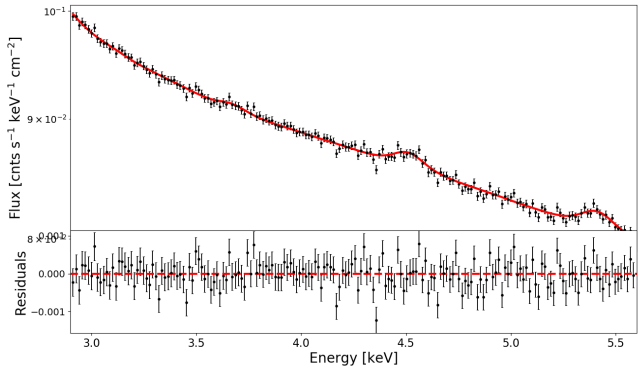


Figure 8. Without removing point-sources: Background-modeled spectrum stacked from all observations in the data set.

4.4.1. *Modeling without the 3.5 keV Line*

Bin	$I_{3.51}$ **Upper-Limit** [10^{-7} ph s^{-1} cm^{-2}]
1	4.45
2	4.67
3	4.54
4	3.42
ALL	2.34

Table 12. Upper-limits on 3.51 keV line flux computed from the non-detections.

The models without a 3.5 keV feature are plotted in Figures 8 and 25 and again produced highly effective fits, achieving a reduced χ^2 of 1.02 for the total data set, with all models exhibiting highly ideal reduced χ^2 values between 0.97 and 1.04. The best-fit parameter values are reported in Table 15.

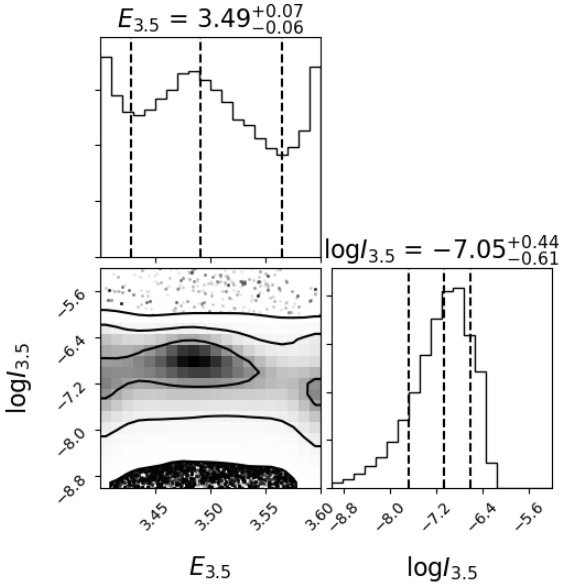


Figure 9. Without removing point-sources: MCMC contour plot for the background-modeled spectrum stacked from all observations with 3.5 keV line energy free to vary between 3.4–3.6 keV.

Bin	χ^2 w/line (DOF=161)	χ^2 w/out (DOF=162)	$\Delta\chi^2$ (ΔDOF=1)	Detection Probability	Line Significance
1	169.07	168.13	-0.94	0.000	0.00σ
2	160.63	160.04	-0.59	0.000	0.00σ
3	164.56	165.06	0.50	0.520	0.71σ
4	157.73	156.89	-0.84	0.000	0.00σ
ALL	165.78	165.21	-0.57	0.000	0.00σ

Table 13. Without removing point-sources: The results of χ^2 testing on background-modeled spectra. Note that DOF denotes degrees of freedom.

Bin	ΔBIC	Evidence **against** Model w/Line	Bayes Factor	Detection Probability	Line Significance
1	11.32	Very Strong	287.25	0.003	0.00σ
2	10.99	Very Strong	244.05	0.004	0.00σ
3	9.84	Strong	137.31	0.007	0.01σ
4	11.23	Very Strong	274.45	0.004	0.00σ
ALL	10.98	Very Strong	242.71	0.004	0.00σ

Table 14. Without removing point-sources: The results of BIC testing on background-modeled spectra. The strength of evidence against the model with a line at 3.51 keV is determined via the standard scale used to qualitatively interpret the ΔBIC and corresponding Bayes Factor, originally established by Kass & Raftery (1995).

Parameter [Unit]	All	Bin 1	Bin 2	Bin 3	Bin 4
Γ_{PL}	$1.63^{+0.01}_{-0.04}$	$1.47^{+0.03}_{-0.02}$	$1.47^{+0.02}_{-0.01}$	$1.47^{+0.03}_{-0.02}$	$1.48^{+0.03}_{-0.02}$
I_{PL} [10^{-4} ph s^{-1} cm^{-2}]	$3.33^{+0.03}_{-0.13}$	$3.21^{+0.1}_{-0.06}$	$3.46^{+0.09}_{-0.06}$	$3.55^{+0.1}_{-0.07}$	$3.45^{+0.11}_{-0.09}$
Γ_{PBK}	$11.28^{+0.02}_{-0.05}$	$12.4^{+0.42}_{-0.63}$	$10.78^{+0.37}_{-0.2}$	$11.67^{+0.59}_{-0.55}$	$11.12^{+0.69}_{-0.44}$
I_{PBK} [ph s^{-1} cm^{-2}]	$13.68^{+0.44}_{-0.01}$	$11.01^{+0.85}_{-0.93}$	$8.56^{+1.04}_{-0.89}$	$12.9^{+1.42}_{-1.74}$	$9.97^{+1.97}_{-1.52}$
$E_{4.5}$ [keV]	$4.52^{+0.01}_{-0.01}$	$4.5^{+0.03}_{-0.03}$	$4.53^{+0.01}_{-0.02}$	$4.52^{+0.01}_{-0.01}$	$4.51^{+0.02}_{-0.02}$
$I_{4.5}$ [10^{-7} ph s^{-1} cm^{-2}]	$8.1^{+0.55}_{-0.54}$	$6.37^{+1.62}_{-2.37}$	$9.02^{+2.08}_{-1.92}$	$9.69^{+1.81}_{-1.86}$	$7.35^{+1.78}_{-1.78}$
$E_{5.4}$ [keV]	$5.42^{+0.01}_{-0.01}$	$5.42^{+0.02}_{-0.02}$	$5.41^{+0.01}_{-0.01}$	$5.43^{+0.01}_{-0.01}$	$5.4^{+0.01}_{-0.01}$
$I_{5.4}$ [10^{-7} ph s^{-1} cm^{-2}]	$14.39^{+0.77}_{-1.21}$	$13.33^{+2.84}_{-3.31}$	$18.47^{+3.09}_{-2.94}$	$13.57^{+3.1}_{-2.7}$	$13.49^{+3.18}_{-2.81}$
E_1 [keV]	$2.69^{+0.01}_{-0.04}$	$2.63^{+0.05}_{-0.07}$	$2.61^{+0.07}_{-0.08}$	$2.63^{+0.05}_{-0.07}$	$2.58^{+0.08}_{-0.06}$
σ_1 [keV]	$0.47^{+0.05}_{-0.0}$	$0.44^{+0.08}_{-0.05}$	$0.45^{+0.05}_{-0.05}$	$0.53^{+0.06}_{-0.06}$	$0.49^{+0.05}_{-0.05}$
I_1 [10^{-2} ph s^{-1} cm^{-2}]	$0.58^{+0.1}_{-0.01}$	$0.57^{+0.1}_{-0.08}$	$0.68^{+0.14}_{-0.12}$	$0.72^{+0.11}_{-0.09}$	$0.77^{+0.11}_{-0.12}$
E_2 [keV]	$2.16^{+0.0}_{-0.0}$	$2.16^{+0.0}_{-0.0}$	$2.16^{+0.0}_{-0.0}$	$2.16^{+0.0}_{-0.0}$	$2.16^{+0.0}_{-0.0}$
σ_2 [10^{-2} keV]	$4.67^{+0.01}_{-0.02}$	$4.57^{+0.09}_{-0.09}$	$4.57^{+0.06}_{-0.06}$	$4.68^{+0.05}_{-0.05}$	$4.72^{+0.07}_{-0.07}$
I_2 [10^{-2} ph s^{-1} cm^{-2}]	$2.47^{+0.0}_{-0.01}$	$2.13^{+0.03}_{-0.03}$	$2.76^{+0.02}_{-0.02}$	$2.61^{+0.02}_{-0.02}$	$2.41^{+0.02}_{-0.02}$
E_3 [keV]	$2.52^{+0.0}_{-0.0}$	$2.48^{+0.01}_{-0.01}$	$2.52^{+0.01}_{-0.01}$	$2.52^{+0.01}_{-0.01}$	$2.52^{+0.01}_{-0.01}$
σ_3 [keV]	$0.17^{+0.0}_{-0.0}$	$0.2^{+0.02}_{-0.02}$	$0.16^{+0.01}_{-0.01}$	$0.17^{+0.01}_{-0.01}$	$0.16^{+0.01}_{-0.01}$
I_3 [10^{-2} ph s^{-1} cm^{-2}]	$0.59^{+0.01}_{-0.02}$	$0.52^{+0.09}_{-0.07}$	$0.54^{+0.06}_{-0.06}$	$0.61^{+0.04}_{-0.05}$	$0.5^{+0.06}_{-0.06}$
E_4 [keV]	$2.67^{+0.33}_{-0.02}$	$3.03^{+0.21}_{-0.31}$	$2.95^{+0.26}_{-0.29}$	$2.96^{+0.24}_{-0.3}$	$3.05^{+0.2}_{-0.35}$
σ_4 [keV]	$10.44^{+0.14}_{-0.61}$	$14.34^{+3.93}_{-2.78}$	$17.32^{+1.83}_{-2.68}$	$16.52^{+2.39}_{-3.36}$	$16.78^{+2.24}_{-2.71}$
I_4 [ph s^{-1} cm^{-2}]	$2.07^{+0.02}_{-0.13}$	$2.39^{+0.64}_{-0.46}$	$3.58^{+0.37}_{-0.55}$	$3.31^{+0.47}_{-0.67}$	$3.12^{+0.41}_{-0.5}$
$I_{3.7}$ [10^{-5} ph s^{-1} cm^{-2}]	$7.88^{+0.48}_{-1.87}$	$10.32^{+6.99}_{-5.21}$	$8.57^{+5.78}_{-5.4}$	$7.05^{+4.9}_{-3.98}$	$7.32^{+6.46}_{-4.14}$
$I_{3.3}$ [10^{-5} ph s^{-1} cm^{-2}]	$0.00^{+0.00}_{-0.00}$	$3.06^{+5.48}_{-1.43}$	$0.00^{+0.00}_{-0.00}$	$0.82^{+2.8}_{-0.32}$	$6.24^{+4.58}_{-3.2}$

Table 15. Without removing point-sources: Best-fit model parameters for the background-modeled spectra with 1σ errors. The astrophysical parameters are reported in the upper panel, while particle background parameters are reported in the lower panel.

Here, regarding the features at 3.3 keV and 3.68 keV, we find results consistent with those of the source-removed data described in section 4.3.3. The 3.68 keV

Bin	$I_{3.51}$ [10^{-7} ph s^{-1} cm^{-2}]
1	$0.86^{+1.10}_{-0.62}$
2	$0.94^{+1.05}_{-0.66}$
3	$1.40^{+1.14}_{-0.90}$
4	$0.83^{+1.02}_{-0.60}$
ALL	$0.47^{+0.52}_{-0.33}$

Table 16. Without removing point-sources: Best-fit 3.51 keV line flux for each background-modeled spectrum with 1σ errors.

feature exhibits a slightly higher flux and comparable significance ($\sim 4\sigma$ in the total data set), again thoroughly refuting the fiducial Dessert et al. (2020) analysis that omitted the feature. This is also consistent with the hypothesis that the feature is at least largely instrumental. We again find a low flux for the 3.3 keV line in all models, except in bin 1 where its flux is greater by a factor of ~ 5. While the 3.3 keV feature in bin 1 still has a low flux that is considerably lower than the 3.68 keV line flux in the same bin, its higher value in that region may be related to the bin's proximity to the Galactic Center, possibly containing traces of baryonic material and hence remaining consistent with the hypothesis that it is largely astrophysical.

4.4.2. *Free-to-vary 3.5 keV Line Energy*

The parameter value distributions and contour plots for 3.5 keV line energy and normalization are shown in Figures 9 and 26. In this case, the total data set exhibits a small peak at ~ 3.5 keV in the line energy distribution. Bins 1 and 4 again have low line energy probability densities around 3.5 keV, with bin 2 showing the same behavior, unlike in the source-removed analysis. Bin 3 displays the sharpest ~ 3.5 keV peak of line energy probability density seen in this work, with the peak occurring at 3.51 keV (which, as mentioned, is among the justifications for our choice of fixed line energy when assessing significance and setting upper-limits). These results lead to the preliminary conclusions that there is a non-detection in bins 1, 2, and 4, while there may be features in bin 3 and in the total data set, and hence we fix line energy at 3.51 keV to assess these hypotheses.

4.4.3. *Fixed 3.5 keV Line Energy*

The line flux probability densities yielded by MCMC are given in Figures 10 and 27, with the best-fit values and 1σ errors reported in Table 16. Using these best-fit values, we can evaluate the statistical significance of the possible feature in all spectra.

4.4.4. *Chi-Squared Testing*

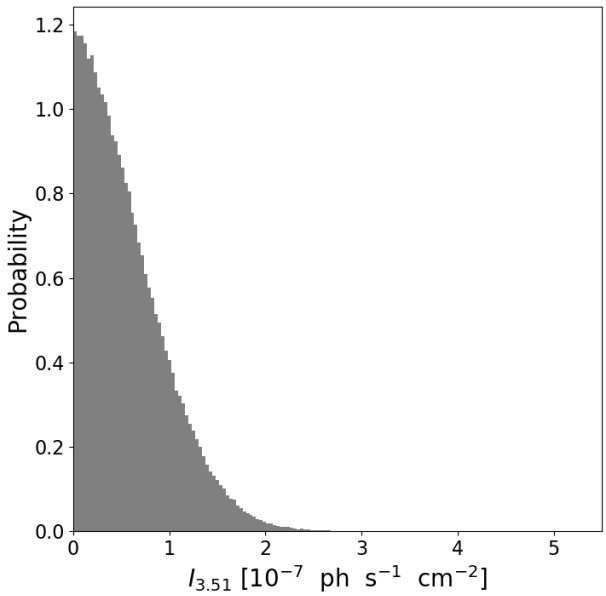


Figure 10. Without removing point-sources: Probability density distribution for 3.51 keV line flux in the spectrum stacked from the total data set.

The results of the χ^2 testing are reported in Table 13. The feature exhibits zero statistical significance in the total data set and in all bins, except bin 3. There, the significance is estimated using $\Delta\chi^2$ to be 0.71σ, suggesting the possible feature is consistent only with a statistical fluctuation.

4.4.5. *BIC Testing*

The BIC testing results are reported in Table 14. The feature again displays zero statistical significance in the total data set and in all bins, except bin 3. In this case, ΔBIC estimates the significance to be 0.01σ, again consistent only with a statistical fluctuation.

4.4.6. *Upper-Limits*

Considering the χ^2 and BIC testing results together allows us to conclude non-detections in all source-intact spectra. We hence follow our procedure of obtaining upper-limits on line flux via the upper 3σ confidence bound on the line flux probability distribution. The upper-limits, in units of 10^{-7} ph s^{-1} cm^{-2}, are 4.96, 4.59, 5.01, and 4.53 in bins 1 through 4 respectively, and 2.27 in the total data set. These are consistent with the upper-limits set by the source-removed data within up to $\sim 11\%$ in bins 1 through 3, and within $\sim 32\%$ in bin 4. The upper-limit for the total data set matches the source-removed upper-limit within $\sim 3\%$, further reinforcing the results.

5. DISCUSSION

Here we offer an interpretation of the analysis results and a comparison between the surface brightness profile of the line flux's upper-limits and the predicted NFW flux. Additionally, we constrain the ∼7 keV sterile neutrino mixing angle and decay rate to compare with previous works.

5.1. *Interpretation of Results*

As mentioned earlier, the background-subtracted results are substantially less statistically viable than the background-modeled results, due to the heavily reduced statistics and the observed background artifact at ∼3.5 keV. Therefore, to ensure a thorough interpretation using the full statistics of our ∼51 Ms of data, we will draw conclusions only from the background-modeled results.

When 3.5 keV line energy was left free to vary, some spectra yielded very low line flux probability densities around 3.5 keV suggesting non-detections, while others exhibited marginal peaks at ∼3.5 keV suggesting a possible feature. Significance testing via both the χ^2 and BIC methods confirmed hypothesized non-detections and showed that all potential 3.5 keV features are consistent only with statistical fluctuations. These results were decisively solidified by applying the same procedure to the source-intact data, allowing us to reach the confident conclusion that no 3.5 keV emission feature was detected in this work. Furthermore, as we considered increasingly high-statistics data, we saw a general decrease in significance estimates via both methods of testing, reinforcing the evidence that any 3.5 keV feature in our data is merely a statistical fluctuation. We can thus use our non-detections to constrain the line flux radial profile, so we choose the upper-limits set by the source-removed analysis. As discussed, those upper-limits are closely consistent with the upper-limits set by the source-intact data. Our choice to utilize the source-removed upper-limits is due to fact that the source-removed data is free of virtually all sources and hence contains minimal foreground signals, allowing for a more thorough and reliable application to the Dark Matter Halo.

5.2. *Comparison to Dessert et al. 2020*

While the fiducial upper-limits set by Dessert et al. (2020) have been questioned in part due to the omission of the 3.3 keV and 3.68 keV lines in the analysis, the publication provided supplemental materials detailing an additional modeling process. This supplemental model accounts for the 3.3 keV and 3.68 keV lines, finding a new upper-limit on the $\sin^2(2\theta)$ a factor of ∼8 times higher than that of the fiducial analysis. Boyarsky et al. (2020) finds results consistent with this supplemental upper-limit. Abazajian (2020) argues the true upper-limit may exceed the fiducial upper-limit by a factor of ∼20 or more, and Boyarsky et al. (2020) supports this claim, pointing out that the reliance of the constraint on local dark matter density introduces a systematic uncertainty of up to a factor of 3 on even the supplemental constraint. Furthermore, as discussed in sections 4.3.3 and 4.4.1, the 3.68 keV line was detected at high significance in our total data set, at 4.06σ in the source-removed data and at 3.58σ in the source-intact data. This suggests the feature is highly significant and hence our results thoroughly refute the fiducial Dessert et al. (2020) constraints found using models that fail to account for the 3.68 keV feature. Thus, when comparing our results to Dessert et al. (2020), we will henceforth exclusively consider that work's higher supplemental upper-limit in favor of its reported fiducial constraint. The supplemental upper-limit will be referred to as the *XMM-Newton* Milky Way Halo upper-limit to avoid confusion with results of the Dessert et al. (2020) fiducial analysis.

5.3. *Radial Profile of 3.5 keV Line Flux*

To constrain the decaying dark matter scenario of the 3.5 keV line, we compare the upper-limit flux distribu-

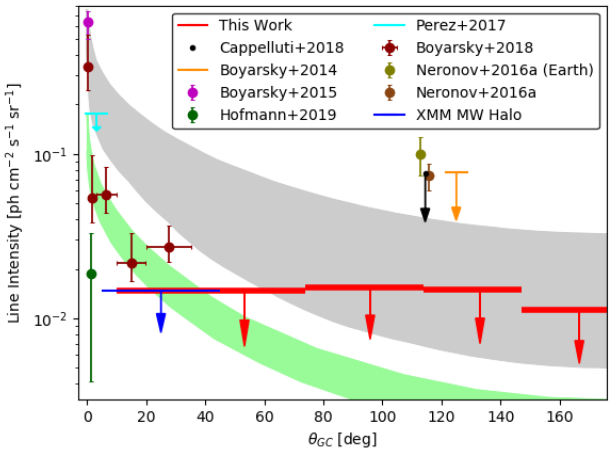


Figure 11. The surface brightness profile of the 3.5 keV line upper-limits. The gray extended curve indicates our NFW profile's 2σ bounds. The green extended curve represents the 2σ bounds of the McMillan (2017) NFW profile used in Boyarsky et al. (2018). Red arrows indicate upper-limits from this work, with each arrow plotted at the average position of observations in the corresponding bin. The blue arrow represents the *XMM-Newton* Milky Way Halo upper-limit. Horizontal error bars indicate the angular distances contained in a given bin.

tion to the predicted line flux profile for the Milky Way's Dark Matter Halo by the Navarro-Frenk-White (NFW) distribution of dark matter (Navarro et al. 1997). Here, we follow the NFW profile method of Cappelluti et al. (2018), similar to that which was later used by Boyarsky et al. (2018). According to the NFW surface brightness profile, the line intensity should be given by

$$I_\nu(\theta_{GC}) = I_{DM,GC} \frac{\int \rho_{NFW}[r(l,0°)] dl d\Omega}{\int \rho_{NFW}[r(l,\theta_{GC})] dl d\Omega} \quad (2)$$

where $I_{DM,GC}$ is the expected dark matter decay signal from the Galactic Center and is empirically determined (Cappelluti et al. 2018). Here, the radial distance from the galactic center (r) is formulated as a function of the distance along the line of sight (l) and the angular distance from the Galactic Center (θ_{GC}). This formulation and integration shown above must be performed to account for all contributions from decaying dark matter along the line of sight. The function r, its variables l and θ_{GC}, and the distance from the Galactic Center to Earth (d) are related by the Law of Cosines, given by:

$$r(l,\theta_{GC}) = \sqrt{l^2 + d^2 - 2ldcos(\theta_{GC})} \quad (3)$$

The NFW profile, describing the density of dark matter halos as a function of distance from their respective galactic centers ($\rho_{NFW}(r)$ in Equation 2) is established by Navarro et al. (1997) as

$$\rho_{NFW}(r) = \frac{\rho_0}{\frac{r}{R_s}\left(1 + \frac{r}{R_s}\right)} \quad (4)$$

and is formulated in (2) as $\rho_{NFW}[r(l,\theta_{GC})]$, a functional of $r(l,\theta_{GC})$. The ρ_0 and scale radius (R_s) parameters are galaxy-specific, and their exact values in the Milky Way are still contested (Bland-Hawthorn & Gerhard 2016). Like Cappelluti et al. (2018), we have opted to primarily use the parameters measured by Nesti & Salucci (2013), i.e., $R_s \sim 16$ kpc with a local dark matter density $\rho_\odot \sim 0.67$ GeV cm^{-3} at solar position $r_\odot \sim 8.0$ kpc (Table 17). The resulting NFW profile is plotted with data from various prior works in Figure 11, where the McMillan (2017) NFW profile adopted in Boyarsky et al. (2018) to optimize its correspondence to that work's data (using the conventionally-approximated $R_s = 20$ kpc in contrast to our empirical R_s, and a more conservative dark matter density $\rho_\odot \sim 0.4$ GeV cm^{-3} at solar position $r_\odot \sim 8.1$ kpc) is also shown.

The upper-limits appear marginally consistent with the empirical Nesti & Salucci (2013) NFW profile, though the profile appears to more closely resemble a zero-slope line. This is consistent with a wholly non-existent feature whose upper-limits have no dependence on radial position in the Milky Way, but rather on the procedure responsible for generating the line flux probability distribution. Moreover, the upper-limit set in bin 1 is in exact agreement with the *XMM-Newton* Milky Way Halo upper-limit. The possible detection in Cappelluti et al. (2018) finds a flux considerably higher than our upper-limits in the region, and hence we plot the reported upper-limit from that work, to which our results offer heavy further constraints. Our upper-limits also firmly exclude the *NuSTAR* fluxes, strongly evidencing the hypothesis that the *NuSTAR* detections are instrumental effects.

Parameter [Units]	Value
d [kpc]	$8.02^{+0.2}_{-0.2}$
ρ_0 [10^6 M$_\odot$ kpc^{-3}]	$13.8^{+20.7}_{-6.6}$
R_s [kpc]	$16.10^{+12.2}_{-5.6}$
$I_{DM,GC}$ [ph s^{-1} cm^{-2} sr^{-1}]	$0.63^{+0.11}_{-0.11}$

Table 17. Milky Way Dark Matter Halo parameters used in Figure 11, originally measured by Nesti & Salucci (2013).

However, due to the wide range of angular distances contained in each bin, our flux profile lacks the spatial resolution to evaluate whether it matches the NFW profile throughout the galaxy, particularly the highly marginal consistency seen in bin 1. Furthermore, the systematic uncertainty introduced by the choice of model parameters prevents us from excluding correspondence to all NFW profiles, such as the McMillan (2017) profile shown in Figure 11. Dark matter may follow a profile other than NFW (see Burkert 1995, Einasto 1965, Read et al. 2016, Abazajian et al. 2020a, and others referenced therein for extensive discussions), rendering an NFW profile comparison model-dependent and not entirely conclusive. Therefore, despite our strong constraints, we cannot definitively rule out the decaying dark matter interpretation of the 3.5 keV line based on the radial profile of its upper-limits.

5.3.1. *Profile Comparison to Boyarsky et al. 2018*

Figure 11 appears to show tension between our results and those of Boyarsky et al. (2018), in which the positions of two data points fall within this work's bin 1. In particular, it appears that the two outer regions analyzed by Boyarsky et al. (2018) exhibit a 3.5 keV line flux that is excluded by our bin 1 upper-limit. This, however, is not the case, and in fact our results are consistent with Boyarsky et al. (2018).

While the two overlapping data points from Boyarsky et al. (2018) are clearly above our bin 1 upper-limit in the figure, they are comparable values, with the lower 1σ error bound of the inner point differing from our con-

straint only by ∼15%. When making such close comparisons towards a spatial boundary of our bin, the coarseness of the bin must be taken into consideration. As described in section 3, the bin sizes were chosen to include enough exposure time for a significant detection of the 3.5 keV line. As a result, the bins span large distances, across which the predicted NFW dark matter density can vary considerably. While providing the best possible flux upper-limit profile given the limitations of the available data, and thus allowing the most robust possible comparison to NFW predictions, the width of the bins do not yield accurate comparisons to nearby data points at their boundaries, such as the Boyarsky et al. (2018) points in question. Bin 1, for example, contains data from between 10 and 74 degrees of angular distance from the Galactic Center, with its constituent observations averaging a distance of 53.3 degrees, while data from the two Boyarsky et al. (2018) points comes exclusively from the region between 10 and 35 degrees from the Galactic Center. Therefore, a more thorough comparison is necessary.

To perform this comparison, we use the best-fit decay rate from Boyarsky et al. (2018), obtained in that work via the entirety of its data set. Assuming the NFW profile employed in that work (represented by the light green region in Figure 11) and using the relation between flux and decay rate given by Equation 5 (found below in section 5.4), we can compute the expected 3.5 keV line flux in bin 1. The results of this computation are shown and compared to our bin 1 upper-limit in Figure 12, which shows consistency between our results.

This consistency is reinforced when considering the differences between our data set and that of Boyarsky et al. (2018). Here, we exclude the Galactic Disc, whereas a considerable portion of the Boyarsky et al. (2018) data set is dominated by the Galactic Disc. While dark matter profiles such as NFW describe a spherically-symmetric dark matter halo, it has been speculated that disc galaxies such as the Milky Way each have a "dark disc" such that the galaxy's galactic disc contains a higher dark matter density than otherwise predicted by spherical dark matter profiles (Read et al. 2008; Bruch et al. 2009; Read et al. 2010; Read 2014). In particular, Bruch et al. (2009) attempted to measure the density of the Milky Way's dark disc, finding that, in Earth's local region of the disc, the dark matter density could be 20–100% more dense than the portion of the Dark Matter Halo outside the Galactic Disc at the same distance from the Galactic Center. In the case of the 3.5 keV line's decaying dark matter interpretation, this would produce a correspondingly higher line flux in a data set that includes the Galactic Disc, such as that of Boyarsky et al. (2018), than in a data set that excludes the Galactic Disc such as ours.

Accounting for cross-calibration between *XMM-Newton* (used in Boyarsky et al. 2018) and *Chandra* further strengthens the agreement between our results. All putative 3.5 keV emission occurs in the hard band (2–7 keV), in which *XMM-Newton* fluxes tend to be greater than those of *Chandra* by ∼5–10%, as shown by Nevalainen et al. (2010) and thoroughly supported by Schellenberger et al. (2015). Therefore, considering this and all other aspects of the comparison between this work and Boyarsky et al. (2018), we thus reach the robust conclusion that our results are consistent.

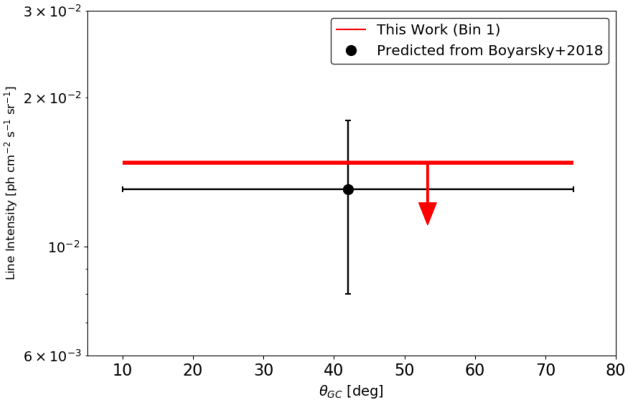


Figure 12. Comparing this work's upper-limit in bin 1 (see Figure 11) to a 3.5 keV line flux prediction made using data from Boyarsky et al. (2018). The predicted flux uses the best-fit dark matter decay rate computed in Boyarsky et al. (2018) from that work's total data set, located at angular distances within 35 degrees from the Galactic Center, together with the NFW profile used in that work (represented by the light green region in Figure 11) to yield the expected 3.5 keV line flux in this work's bin 1.

5.4. *Constraints on Sterile Neutrino Mixing Angle*

In addition to further constraining the sterile neutrino dark matter parameter space, determining the mixing angle associated with our flux upper-limits allows us to directly compare our results from the Milky Way Halo with the results of works from extra-galactic sources such as galaxies and clusters. Total dark matter mass in the FOV must be considered to calculate the mixing angle from line flux, and therefore the value for a Milky Way Halo analysis such as ours is dependent on the choice of dark matter profile. Thus, we have employed a careful procedure to account for this model-dependent uncertainty in our calculation of the mixing angle upper-limit.

For our computation, we use the sterile neutrino decay rate from Pal & Wolfenstein (1982) (Γ_γ; see Equation 1), the empirical Nesti & Salucci (2013) NFW profile, and the predicted flux of decaying dark matter contained in the FOV, given by Neronov et al. (2016b) as:

$$F_{DM} = \frac{\Gamma_\gamma}{4\pi m_s} \frac{M_{DM,FOV}}{D^2} \quad (5)$$

where Γ_γ is the decay rate given in Equation 1, m_s is sterile neutrino mass, $M_{DM,FOV}$ is the total mass of dark matter contained in the FOV, and D is the distance from Earth to the mass of dark matter. From this, one can solve for the factor $\sin^2(2\theta)$, where θ is the mixing angle, which becomes the only variable quantity in Γ_γ when m_s is known (or, in this case, set to $m_s = 2E_{3.51} = 7.02$ keV from the model's fixed line energy), obtaining:

$$sin^2(2\theta) = \frac{F_{3.5}}{C_\Gamma} \frac{1}{m_s^4} \left(\frac{M_{DM,FOV}}{D^2} \right)^{-1} \quad (6)$$

where $F_{3.5}$ is the 3.5 keV line flux and the constant C_Γ is given by:

$$C_\Gamma = \frac{1.38 \times 10^{-22}}{4\pi} s^{-1} keV^{-5} \quad (7)$$

For a given angular distance from the Galactic Center, the surface mass density factor $\frac{M_{DM,FOV}}{D^2}$ can be obtained by integrating the NFW profile (using Equation 4 and applying the desired angular distance to Equation 3) over the FOV's solid angle and line of sight. Integrating accordingly, out to the virial radius r_{200} =200 kpc (Dehnen et al. 2006)[3] to obtain the surface mass density factor $\frac{M_{DM,FOV}}{D^2}$, then evaluating Equation 6 for the flux in each bin, we can put constraints on the ∼7 keV sterile neutrino mixing angle. The results of this calculation are reported in Table 18. Using the results for $\sin^2(2\theta)$ and the corresponding decay rate (Equation 1), we obtain the average lifetime (τ_{DM}) of the sterile neutrino, also reported in Table 18.

We choose the mixing angle obtained via our most widely spatially-distributed and most statistically robust spectrum in the source-removed data—the ∼51 Ms stack containing the total data set—as our final value to constrain the $\sin^2(2\theta)$, m_s parameter space with an upper-limit of $\sin^2(2\theta) = 2.58 \times 10^{-11}$ at $m_s = 7.01$ keV.

To account for the systematic uncertainty resulting from the choices of R_s and local dark matter density, we performed a second computation, replacing our NFW parameters with the most conservative up-to-date values (detailed in Abazajian et al. 2020a), namely $R_s = 26$ kpc and a local dark matter density $\rho_\odot \sim 0.28$ GeV cm^{-3}.

[3] Note that the choice of r_{200} does not substantially impact the results due to the asymptotic nature of the NFW profile at large radii.

Bin	$\sin^2(2\theta)$ $[10^{-11}]$	Γ_γ $[10^{-28}$ s$^{-1}]$	τ_{DM} $[10^{27}$ s]
1	$2.31^{+0.07}_{-0.04}$	$0.53^{+0.02}_{-0.01}$	$18.91^{+0.81}_{-0.49}$
2	$4.39^{+0.13}_{-0.08}$	$1.00^{+0.04}_{-0.03}$	$9.97^{+0.43}_{-0.26}$
3	$5.69^{+0.16}_{-0.1}$	$1.30^{+0.06}_{-0.03}$	$7.68^{+0.33}_{-0.2}$
4	$4.81^{+0.14}_{-0.08}$	$1.10^{+0.05}_{-0.03}$	$9.10^{+0.39}_{-0.23}$
ALL	$2.58^{+0.07}_{-0.04}$	$0.59^{+0.03}_{-0.02}$	$16.95^{+0.73}_{-0.44}$

Table 18. Upper-limit constraints on the ∼7 keV sterile neutrino mixing angle θ. Values were computed for the total data set using the average distance of all observations from the GC, while values in each bin used the average distance from the GC of observations in that bin. 1σ errors represent propagated uncertainties in parameters used for the calculations. Here, we also report the corresponding sterile neutrino decay rates (Γ_γ) and average lifetimes (τ_{DM}).

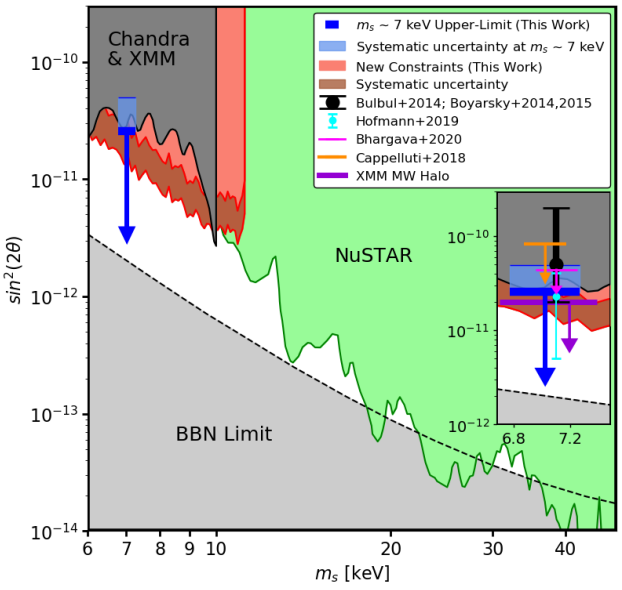


Figure 13. Constraints on the $\sin^2(2\theta)$, m_s parameter space adapted from Roach et al. (2020) and updated with the results of this work. Here, we plot our upper-limit, showing its marginal consistency with previous detections, including Bulbul et al. (2014), Boyarsky et al. (2014), Boyarsky et al. (2015), and moderate consistency with Hofmann & Wegg (2019). For clarity, all previous $m_s \sim 7$ keV data points and upper-limits are shown in a second panel, enlarged for optimal data visualization. Also shown are our additional continuum constraints. Systematic uncertainties on both our $m_s \sim 7$ keV upper-limit and continuum constraints are shown as corresponding shaded regions. Note that a similar figure originally appeared in Ng et al. (2019).

This yielded an upper-limit of $sin^2(2\theta) = 4.96 \times 10^{-11}$, higher than our initial value by a factor of ∼2. The model-dependent uncertainty on the upper-limit is represented in the figure by a shaded region of uncertainty between the two models' upper-limits. Since the Nesti & Salucci (2013) parameters yield a fairly strong profile, the true value likely falls between its resulting upper-limit and that produced by the ultra-conservative Abazajian et al. (2020a) parameters. The McMillan (2017) profile, for example, yields an upper-limit of $sin^2(2\theta) = 3.85 \times 10^{-11}$, falling almost exactly in the middle of our uncertainty region.

5.4.1. *Continuum Constraints on θ and m_s*

We have also added further constraints to the parameter space, derived from the fact that we did not observe any new, unidentified emission lines in our analysis of the 2.9–5.6 keV energy band. To compute these constraints, we simulated spectra in XSPEC from the model of our total data set and with exposure time equal to the data set's total exposure time. For each simulation, we added a faint emission line ($I = 10^{-8}$ ph s^{-1} cm^{-2}) at a given energy on the continuum. The significance of the line was then computed using the $\Delta\chi^2$ test. This process was repeated for the same energy, gradually increasing the flux by 5×10^{-10} ph s^{-1} cm^{-2}, until a significance of at least 3σ was obtained. The procedure was performed for all energies on the 2.9–5.6 keV band, spanned by intervals of 50 eV, a value chosen to be smaller than *Chandra*'s energy resolution and hence to avoid gaps in our constraints across the continuum. When computing mixing angles from fluxes, to account for the same systematic effects encountered in section 5.4, we again perform computations for both the Nesti & Salucci (2013) and the Abazajian et al. (2020a) NFW parameters, represented in Figure 13 by a similar region of uncertainty.

5.4.2. *Comparison to Other Works*

We have plotted our ∼7 keV sterile neutrino upper-limit, along with the *XMM-Newton* Milky Way Halo upper-limit (and various recent data points), onto the data presented by Roach et al. (2020) detailing other recent constraints on the $\sin^2(2\theta)$, m_s parameter space (Figure 13). The dark gray upper-limit region represents prior results from *Chandra* and *XMM-Newton* (see Ng et al. 2019, Roach et al. 2020, and others referenced therein), while the green region represents results from *NuSTAR* (all of which are detailed or reported by Ng et al. 2019, Roach et al. 2020, and others referenced therein). The lower-limit region of the parameter space arises from theoretical values derived by Roach et al. (2020) from big bang nucleosynthesis (BBN) and the resulting limit placed on lepton asymmetry per unit entropy density (Dolgov et al. 2002a; Serpico & Raffelt 2005; Laine & Shaposhnikov 2008; Boyarsky et al. 2009b; Venumadhav et al. 2016; Roach et al. 2020). The upper-limit from our analysis is lower than the value obtained from the possible detection in Cappelluti et al. (2018), suggesting that the 3.51 keV feature found in that work is not associated with sterile neutrino dark matter, and hence we again plot that work's upper-limit. Our upper-limit does, however, remain marginally consistent within 1σ errors with Bulbul et al. (2014), Boyarsky et al. (2014), and Boyarsky et al. (2015), and is moderately consistent with Hofmann & Wegg (2019), potentially leaving room for the ∼7 keV sterile neutrino scenario. Additionally, the upper-limit shows consistency with both the *XMM-Newton* Milky Way Halo upper-limit and the Bhargava et al. (2020) constraint, appearing marginally above the *XMM-Newton* Milky Way Halo value and containing the Bhargava et al. (2020) upper-limit within its systematic uncertainty range.

Also plotted in Figure 13 are the new continuum constraints from our simulations, offering tighter restrictions on the parameter space for masses between ∼6 keV and ∼12 keV. except ∼7 keV. While the continuum constraints at ∼7 keV appear lower than the upper-limit set by our 3.5 keV line analysis, the continuum constraints are computed under the assumption that no feature exists at ∼3.5 keV, and hence do not apply to the region of the parameter space at ∼7 keV. Hence, we have plotted all data points, error bars, and upper-limit arrows for $m_s \sim 7$ keV strictly in front of the red continuum constraint region to appropriately break its continuity on the plot.

An important difference between our figure and the original version in Roach et al. (2020) is the omission of the "Milky Way satellite counts" constraints. The values are simulation-dependent and, as detailed by Boyarsky et al. (2019), cannot be used to constrain the sterile neutrino dark matter parameter space (see also Lovell et al. 2017 for further discussion). As seen in the figure, a substantial portion of the parameter space remains allowed, particularly at $m_s \sim 7$ keV. Thus, while the cases for both ∼7 keV sterile neutrino dark matter and the general decaying dark matter scenario for the 3.5 keV line have been considerably narrowed in this work, they cannot be ruled out completely.

5.5. *Closing Remarks*

This work provides the most comprehensive search to date for decaying dark matter in the Milky Way Halo using one of the various existing large archives of current

X-ray telescopes. A follow-up analysis with new technology and data is required to improve the upper-limits reported here. All-sky coverage and comparable grasp in the keV energy range of the *eROSITA* X-ray telescope will improve current constraints from the Milky Way Halo (Merloni et al. 2012; Hofmann & Wegg 2019). The high spectral resolution of observations using *XRISM* and *Athena* are required to measure the velocity dispersion and resolve the 3.5 keV line from nearby astrophysical lines to disentangle the origin of this feature (Zhong et al. 2020; XRISM Science Team 2020).

6. ACKNOWLEDGEMENTS

The authors kindly acknowledge *Chandra* Grant AR-19023B; Paul P. Plucinsky for his assistance in studying the low statistics of the *Chandra* particle background; and the anonymous reviewer who helped improve the original manuscript. Dominic Sicilian acknowledges the University of Miami for supplying funding; Terrance J. Gaetz for helpful discussions on calibration of the *Chandra* particle background; Keith Arnaud for introducing the method of setting random priors for Goodman-Weare MCMC chains in XSPEC; Iacopo Bartalucci for offering further technical insights into modeling the ACIS particle background; Marco Drewes for enlightening discussions on sterile neutrino dark matter; and Kevork Abazajian for beneficial explanations of sterile neutrino oscillation and dark matter profiles in the Milky Way.

Software: Astropy (Astropy Collaboration et al. 2013; Astropy Collaboration et al. 2018), CIAO (Fruscione et al. 2006), corner.py (Foreman-Mackey 2016), Matplotlib (Hunter 2007), NumPy (van der Walt et al. 2011), PyXspec 2.0.3 (Arnaud 2016), XSPEC 12.10.1f (Arnaud 1996)

REFERENCES

Abazajian, K., Fuller, G. M., & Patel, M. 2001, PhRvD, 64, 023501

Abazajian, K., Fuller, G. M., & Tucker, W. H. 2001, ApJ, 562, 593

Abazajian, K. N. 2017, PhR, 711, 1

Abazajian, K. N. 2020, arXiv e-prints, arXiv:2004.06170

Abazajian, K. N., Horiuchi, S., Kaplinghat, M., et al. 2020, PhRvD, 102, 043012

Arnaud, K. A. 1996, Astronomical Data Analysis Software and Systems V, 17

Arnaud, K. A. 2016, AAS/High Energy Astrophysics Division #15, 115.02

Asaka, T., & Shaposhnikov, M. 2005, Physics Letters B, 620, 17

Astropy Collaboration, Robitaille, T. P., Tollerud, E. J., et al. 2013, A&A, 558, A33

Astropy Collaboration, Price-Whelan, A. M., Sipőcz, B. M., et al. 2018, AJ, 156, 123

Bartalucci, I., Mazzotta, P., Bourdin, H., et al. 2014, A&A, 566, A25

Bhargava, S., Giles, P. A., Romer, A. K., et al. 2020, MNRAS, 497, 656

Bland-Hawthorn, J., & Gerhard, O. 2016, ARA&A, 54, 529

Boyarsky, A., Neronov, A., Ruchayskiy, O., et al. 2006, Soviet Journal of Experimental and Theoretical Physics Letters, 83, 133

Boyarsky, A., Neronov, A., Ruchayskiy, O., et al. 2006, PhRvL, 97, 261302

Boyarsky, A., Lesgourgues, J., Ruchayskiy, O., et al. 2009, PhRvL, 102, 201304

Boyarsky, A., Ruchayskiy, O., & Shaposhnikov, M. 2009, Annual Review of Nuclear and Particle Science, 59, 191

Boyarsky, A., Ruchayskiy, O., Iakubovskyi, D., et al. 2014, PhRvL, 113, 251301

Boyarsky, A., Franse, J., Iakubovskyi, D., et al. 2015, PhRvL, 115, 161301

Boyarsky, A., Iakubovskyi, D., Ruchayskiy, O., et al. 2018, arXiv e-prints, arXiv:1812.10488

Boyarsky, A., Drewes, M., Lasserre, T., et al. 2019, Progress in Particle and Nuclear Physics, 104, 1

Boyarsky, A., Malyshev, D., Ruchayskiy, O., et al. 2020, arXiv e-prints, arXiv:2004.06601

Bruch, T., Read, J., Baudis, L., et al. 2009, ApJ, 696, 920

Bulbul, E., Markevitch, M., Foster, A., et al. 2014, ApJ, 789, 13

Bulbul, E., Markevitch, M., Foster, A. R., et al. 2014, arXiv e-prints, arXiv:1409.4143

Bulbul, E., Markevitch, M., Foster, A., et al. 2016, ApJ, 831, 55

Bulbul, E., Foster, A., Brown, G. V., et al. 2019, ApJ, 870, 21

Bulbul, E., Kraft, R., Nulsen, P., et al. 2020, ApJ, 891, 13

Burkert, A. 1995, ApJL, 447, L25

Cappelluti, N., Bulbul, E., Foster, A., et al. 2018, ApJ, 854, 179

Cash, W. 1979, ApJ, 228, 939

Clowe, D., Bradač, M., Gonzalez, A. H., et al. 2006, ApJL, 648, L109

Dehnen, W., McLaughlin, D. E., & Sachania, J. 2006, MNRAS, 369, 1688

Dessert, Christopher and Rodd, Nicholas L., et al. 2020, Science, 367, 6485
Dessert, C., Rodd, N. L., & Safdi, B. R. 2020, arXiv e-prints, arXiv:2006.03974
Dickey, J. M., & Lockman, F. J. 1990, ARA&A, 28, 215
Dodelson, S., & Widrow, L. M. 1994, PhRvL, 72, 17
Dolgov, A. D., & Hansen, S. H. 2002, Astroparticle Physics, 16, 339
Dolgov, A. D., Hansen, S. H., Pastor, S., et al. 2002, Nuclear Physics B, 632, 363
Drewes, M., & Garbrecht, B. 2013, Journal of High Energy Physics, 2013, 96
Drewes, M. 2013, International Journal of Modern Physics E, 22, 1330019-593
Drewes, M., Garbrecht, B., Gueter, D., et al. 2016, Journal of High Energy Physics, 2016, 150
Drewes, M., Garbrecht, B., Klarić, J., et al. 2017, Journal of Physics Conference Series, 012027
Einasto, J. 1965, Trudy Astrofizicheskogo Instituta Alma-Ata, 5, 87
Evans, I. N., Primini, F. A., Glotfelty, K. J., et al. 2010, ApJS, 189, 37
Evans, I. N., Allen, C., Anderson, C. S., et al. 2019, AAS/High Energy Astrophysics Division, 114.01
Foreman-Mackey, D. 2016, The Journal of Open Source Software, 1, 24
Franse, J., Bulbul, E., Foster, A., et al. 2016, ApJ, 829, 124
Fruscione, A., McDowell, J. C., Allen, G. E., et al. 2006, Proc. SPIE, 62701V
Gall, A. C., Foster, A. R., Silwal, R., et al. 2019, ApJ, 872, 194
Garmire, G. P., Bautz, M. W., Ford, P. G., et al. 2003, Proc. SPIE, 28
Grant, C. E., Bautz, M. W., Kissel, S. M., et al. 2005, Proc. SPIE, 201
Gu, L., Kaastra, J., Raassen, A. J. J., et al. 2015, A&A, 584, L11
Hickox, R. C., & Markevitch, M. 2006, ApJ, 645, 95
Hickox, R. C., & Markevitch, M. 2007, ApJ, 671, 1523
Hitomi Collaboration, Aharonian, F., Akamatsu, H., et al. 2017, Nature, 551, 478
Hofmann, F., & Wegg, C. 2019, A&A, 625, L7
Hunter, J. D. 2007, Computing in Science and Engineering, 9, 90
Kajita, T. 1999, Nuclear Physics B Proceedings Supplements, 77, 123
Kass, R. E., Raftery, A. E. 1995, Journal of the American Statistical Association, 90, 430
Kuntz, K. D., & Snowden, S. L. 2000, AAS/High Energy Astrophysics Division #5 5, 32.26
Kuntz, K. D., & Snowden, S. L. 2000, ApJ, 543, 195
Laine, M. & Shaposhnikov, M. 2008, JCAP, 2008, 031
Lovell, M. R., Bose, S., Boyarsky, A., et al. 2017, MNRAS, 468, 4285
McMillan, P. J. 2017, MNRAS, 465, 76
McDonald, A. B., Ahmad, Q. R., Allen, R. C., et al. 2002, Theoretical Physics: MRST 2002, 43
Merloni, A., Predehl, P., Becker, W., et al. 2012, arXiv e-prints, arXiv:1209.3114
Navarro, J. F., Frenk, C. S., & White, S. D. M. 1997, ApJ, 490, 493
Neronov, A., Malyshev, D., & Eckert, D. 2016, PhRvD, 94, 123504
Neronov, A., & Malyshev, D. 2016, PhRvD, 93, 063518
Nesti, F., & Salucci, P. 2013, JCAP, 2013, 016
Nevalainen, J., David, L., & Guainazzi, M. 2010, A&A, 523, A22
Ng, K. C. Y., Roach, B. M., Perez, K., et al. 2019, PhRvD, 99, 083005
Pal, P. B., & Wolfenstein, L. 1982, PhRvD, 25, 766
Perez, K., Ng, K. C. Y., Beacom, J. F., et al. 2017, PhRvD, 95, 123002
Protassov, R., van Dyk, D. A., Connors, A., et al. 2002, ApJ, 571, 545
Read, J., Debattista, V., Agertz, O., et al. 2008, Identification of Dark Matter 2008, 48
Read, J. I., Bruch, T., Baudis, L., et al. 2010, American Institute of Physics Conference Series, 1240, 391
Read, J. I. 2014, Journal of Physics G Nuclear Physics, 41, 063101
Read, J. I., Agertz, O., & Collins, M. L. M. 2016, MNRAS, 459, 2573
Roach, B. M., Ng, K. C. Y., Perez, K., et al. 2020, PhRvD, 101, 103011
Rubin, V. C., & Ford, W. K. 1970, ApJ, 159, 379
Rubin, V. C., Ford, W. K., & Thonnard, N. 1980, ApJ, 238, 471
Ruchayskiy, O., Boyarsky, A., Iakubovskyi, D., et al. 2016, MNRAS, 460, 1390
Schellenberger, G., Reiprich, T. H., Lovisari, L., et al. 2015, A&A, 575, A30
Schwarz, G. 1978, Annals of Statistics, 6, 461
Sekiya, N., Yamasaki, N. Y., & Mitsuda, K. 2016, PASJ, 68, S31
Serpico, P. D. & Raffelt, G. G. 2005, PhRvD, 71, 127301
Shah, C., Dobrodey, S., Bernitt, S., et al. 2016, ApJ, 833, 52
Urban, O., Werner, N., Allen, S. W., et al. 2015, MNRAS, 451, 2447
Venumadhav, T., Cyr-Racine, F.-Y., Abazajian, K. N., et al. 2016, PhRvD, 94, 043515

van der Walt, S., Colbert, S. C., & Varoquaux, G. 2011, Computing in Science and Engineering, 13, 22

Weller, M. E., Beiersdorfer, P., Lockard, T. E., et al. 2019, ApJ, 881, 92

Wik, D. R., Hornstrup, A., Molendi, S., et al. 2014, ApJ, 792, 48

Wit, E., Van den Heuvel, Edwin, & Romeijn, Jan-Willem 2012, American Journal of Botany, 66

XRISM Science Team 2020, arXiv e-prints, arXiv:2003.04962

Zhang, L., Rix, H.-W., van de Ven, G., et al. 2013, ApJ, 772, 108

Zhong, D., Valli, M., & Abazajian, K. N. 2020, arXiv e-prints, arXiv:2003.00148

Zwicky, F. 1933, Helvetica Physica Acta, 6, 110

Zwicky, F. 1937, ApJ, 86, 217

APPENDIX

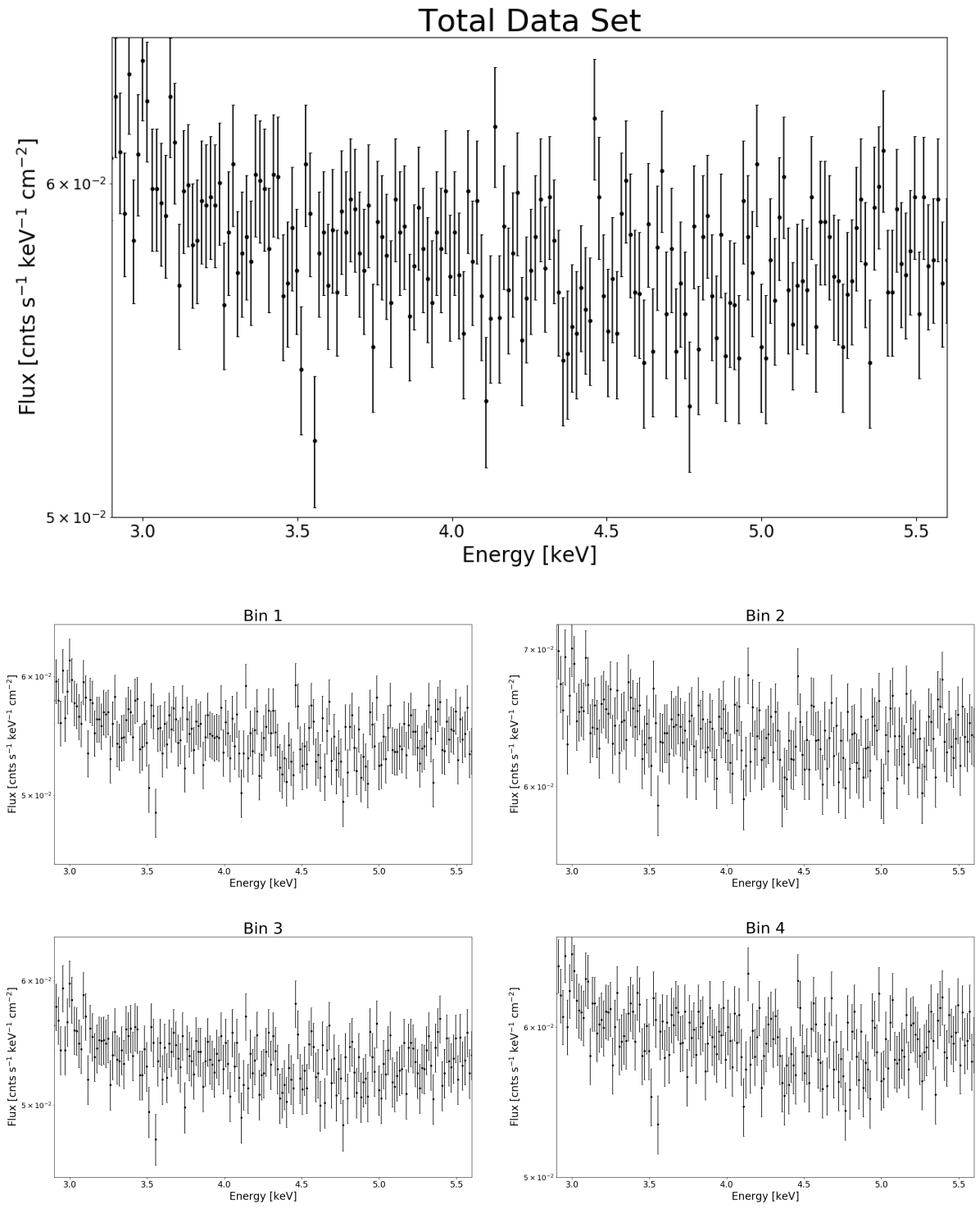


Figure 14. Particle background spectra. Each title indicates to which data spectrum the particle background spectrum corresponds.

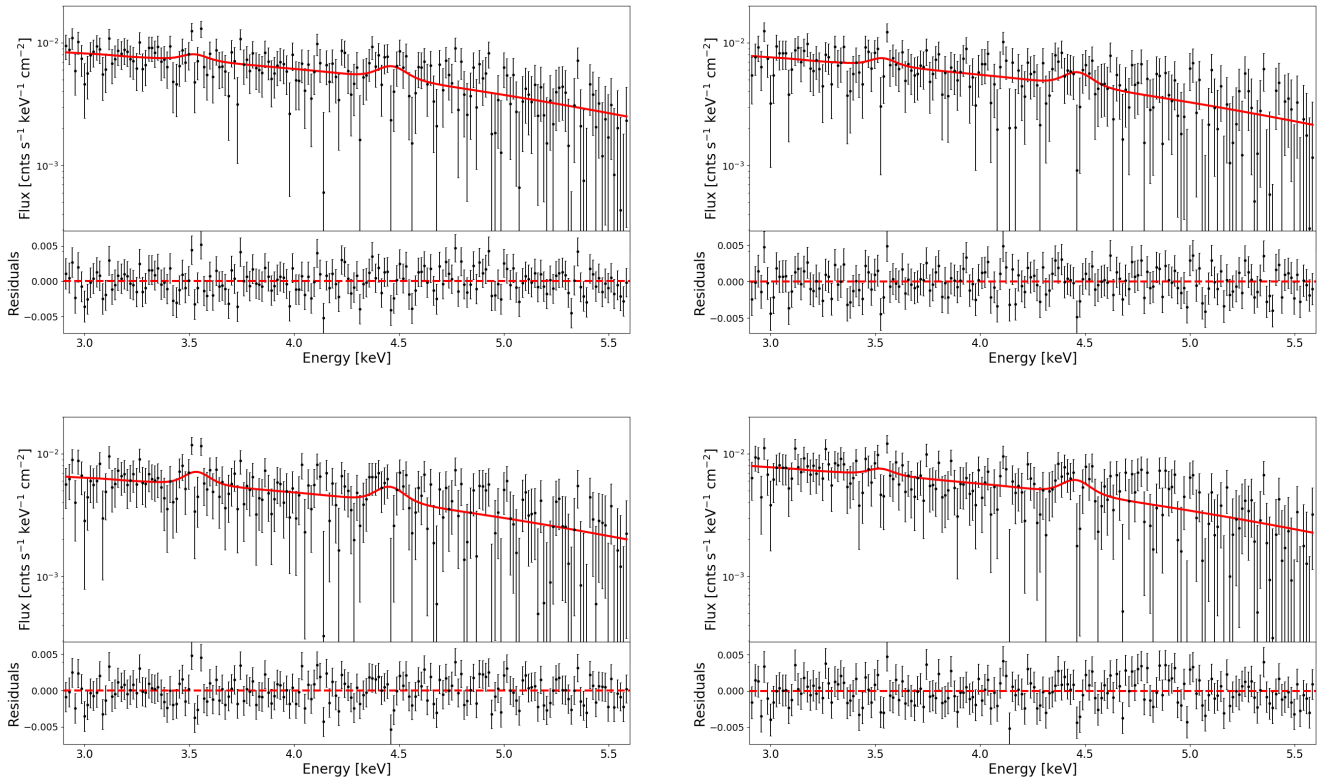


Figure 15. Background-subtracted spectra of each angular distance bin, plotted with the ∼3.5 keV feature modeled. **Top Left:** Bin 1, **Top Right:** Bin 2, **Bottom Left:** Bin 3, **Bottom Right:** Bin 4.

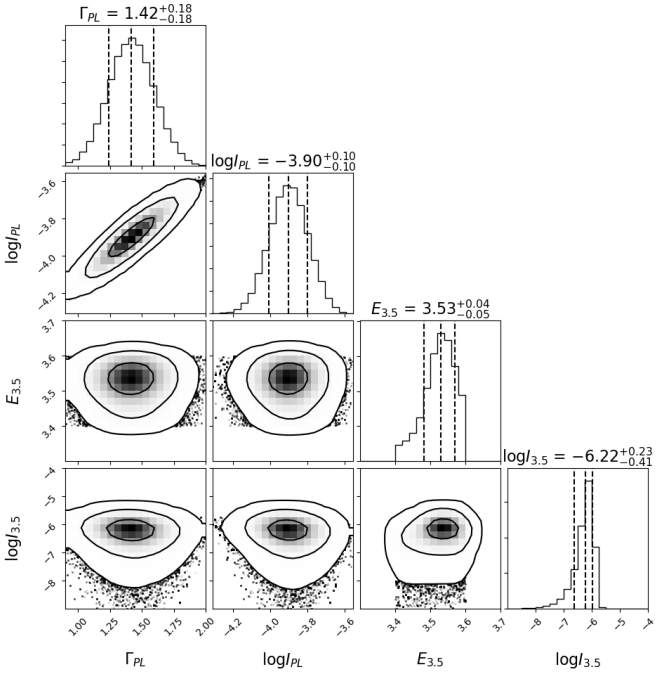


Figure 16. MCMC contour plot for the background-subtracted model of the spectrum containing the total data set.

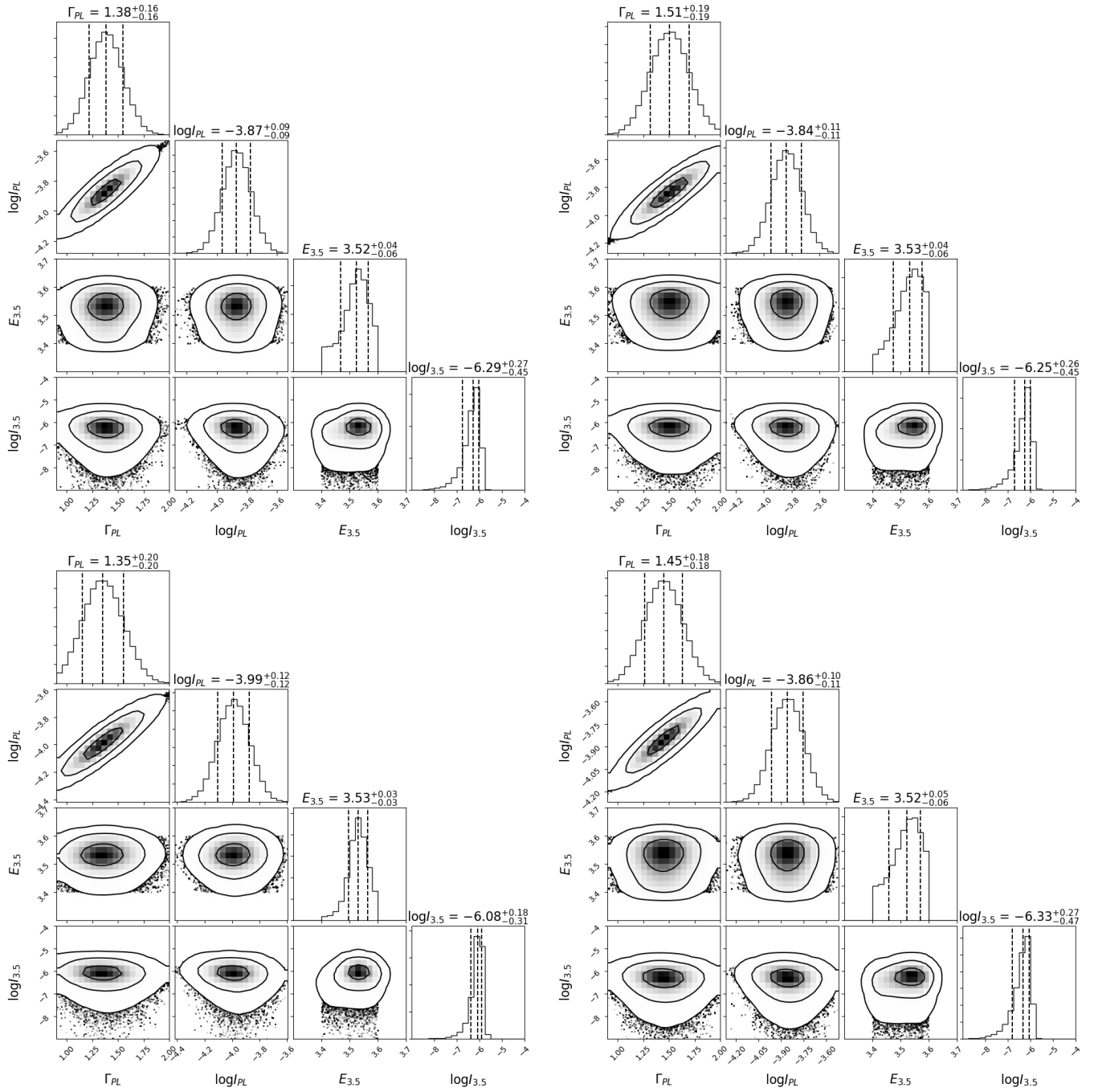


Figure 17. MCMC contour plot for the background-subtracted models. **Top Left:** Bin 1, **Top Right:** Bin 2, **Bottom Left:** Bin 3, **Bottom Right:** Bin 4.

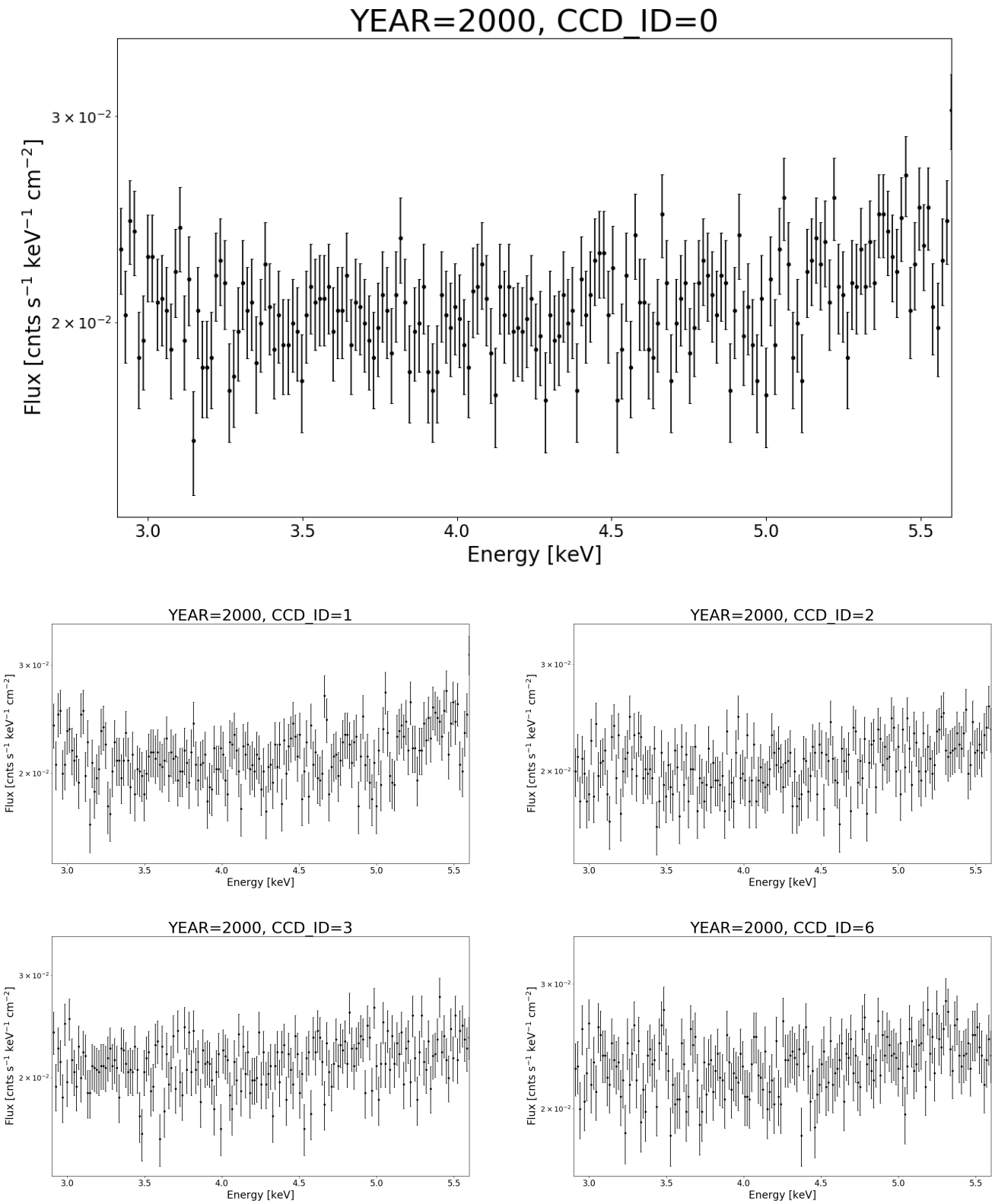


Figure 18. Stowed spectrum for each CCD from the stowed observation in 2000.

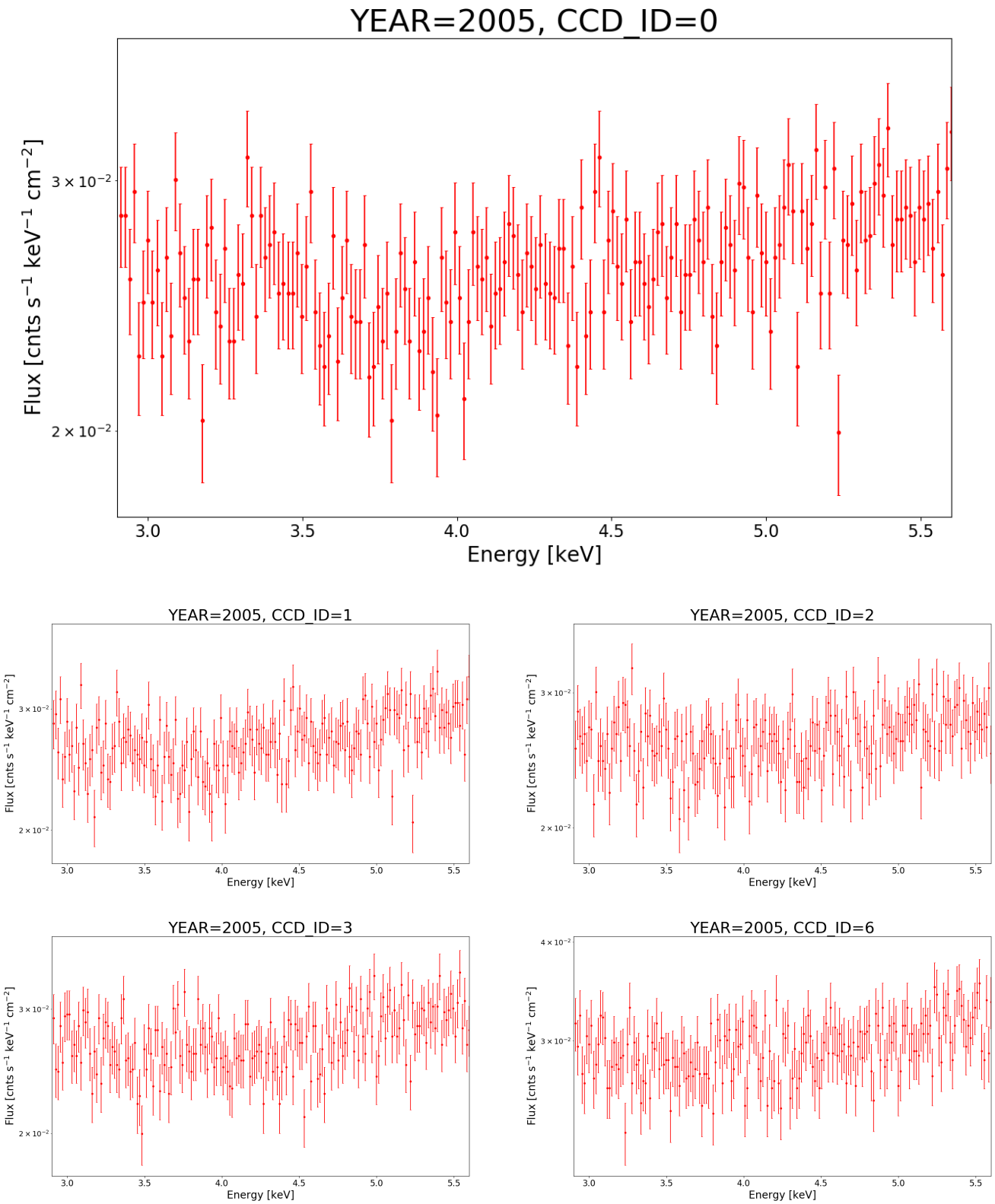


Figure 19. Stowed spectrum for each CCD from the stowed observation in 2005.

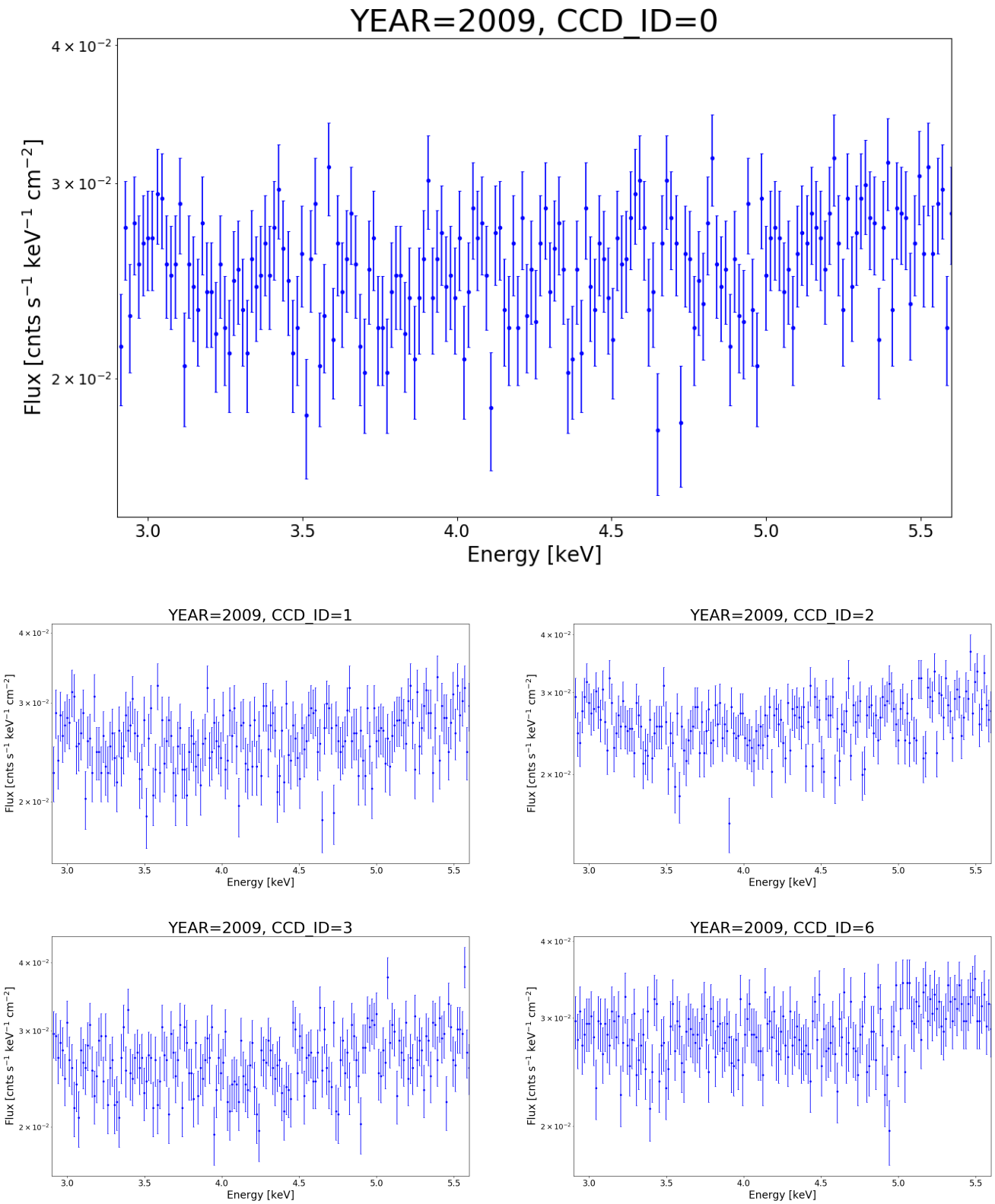


Figure 20. Stowed spectrum for each CCD from the stowed observation in 2009.

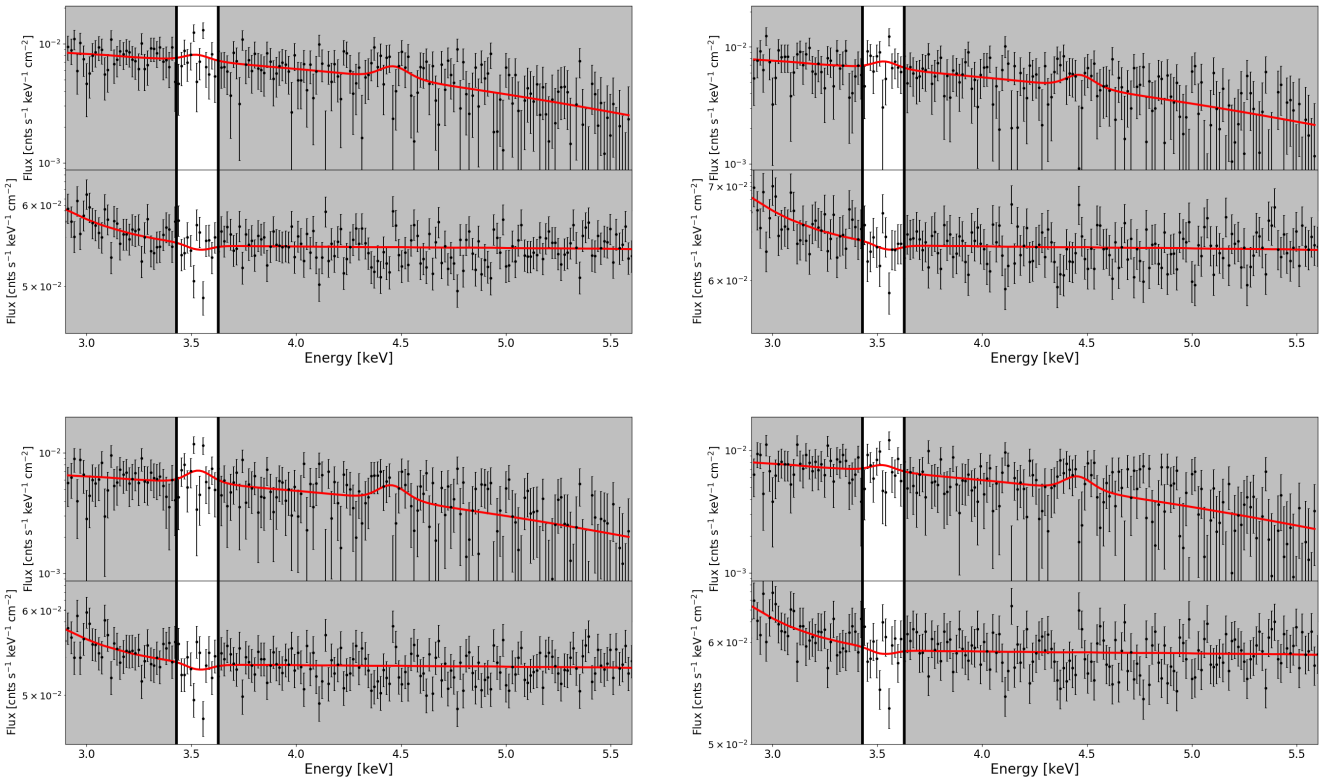


Figure 21. Background-subtracted spectrum of each angular distance bin modeled with a 3.5 keV line, compared to the corresponding background spectrum containing the 3.5 keV dip. These further showcase the correspondence between the anomalous, dipped data points in each background and each background-subtracted spectrum's apparent emission line data points. **Top Left:** Bin 1, **Top Right:** Bin 2, **Bottom Left:** Bin 3, **Bottom Right:** Bin 4.

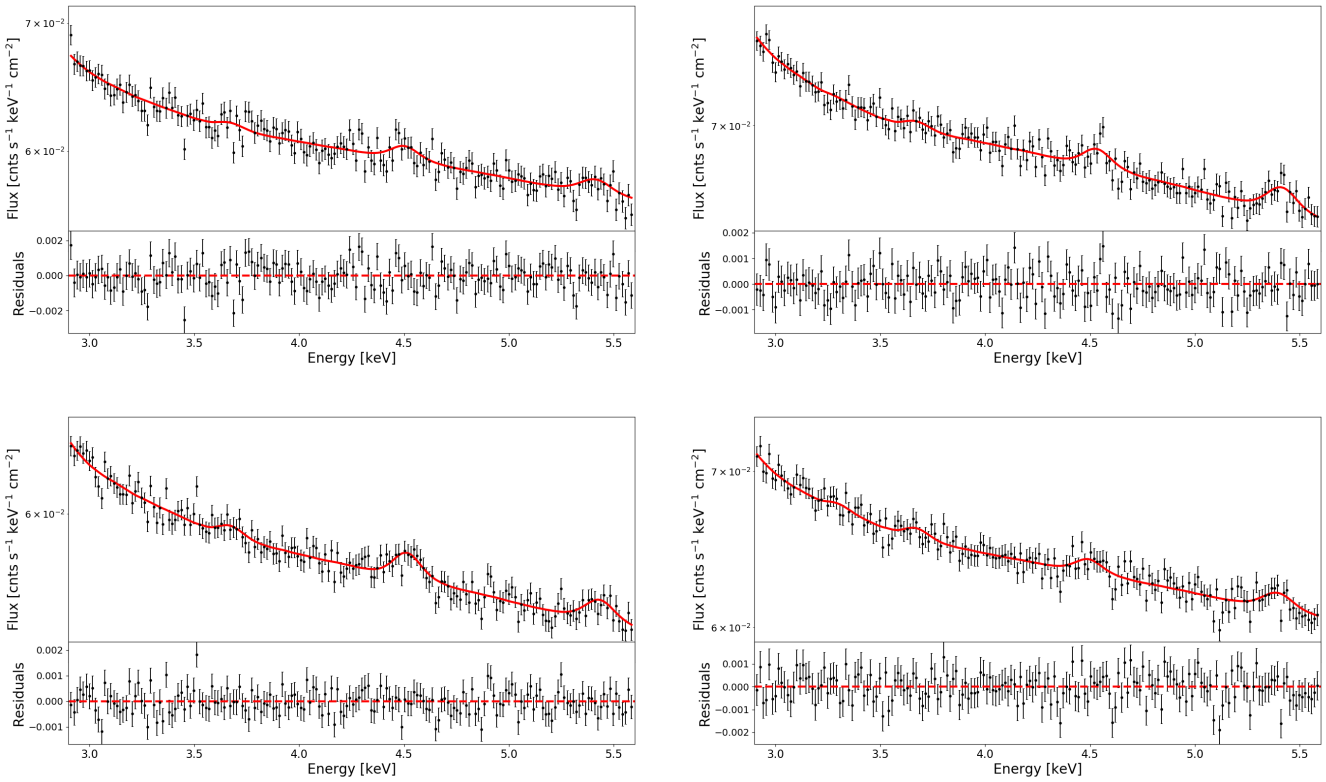


Figure 22. Background-modeled spectra. **Top Left:** Bin 1, **Top Right:** Bin 2, **Bottom Left:** Bin 3, **Bottom Right:** Bin 4.

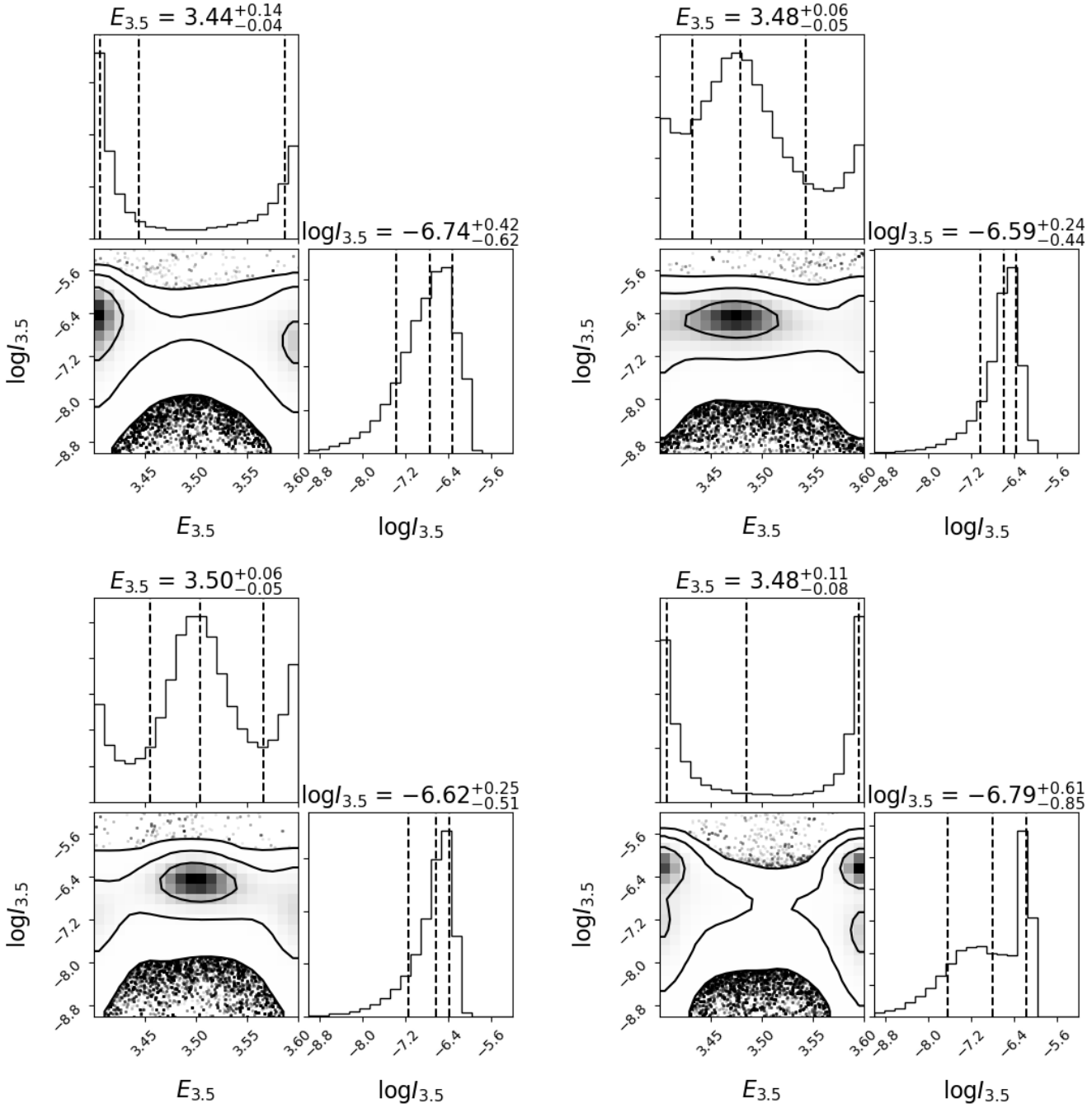


Figure 23. MCMC contour plots for the background-modeled spectra with 3.5 keV line energy free to vary between 3.4–3.6 keV. **Top Left:** Bin 1, **Top Right:** Bin 2, **Bottom Left:** Bin 3, **Bottom Right:** Bin 4.

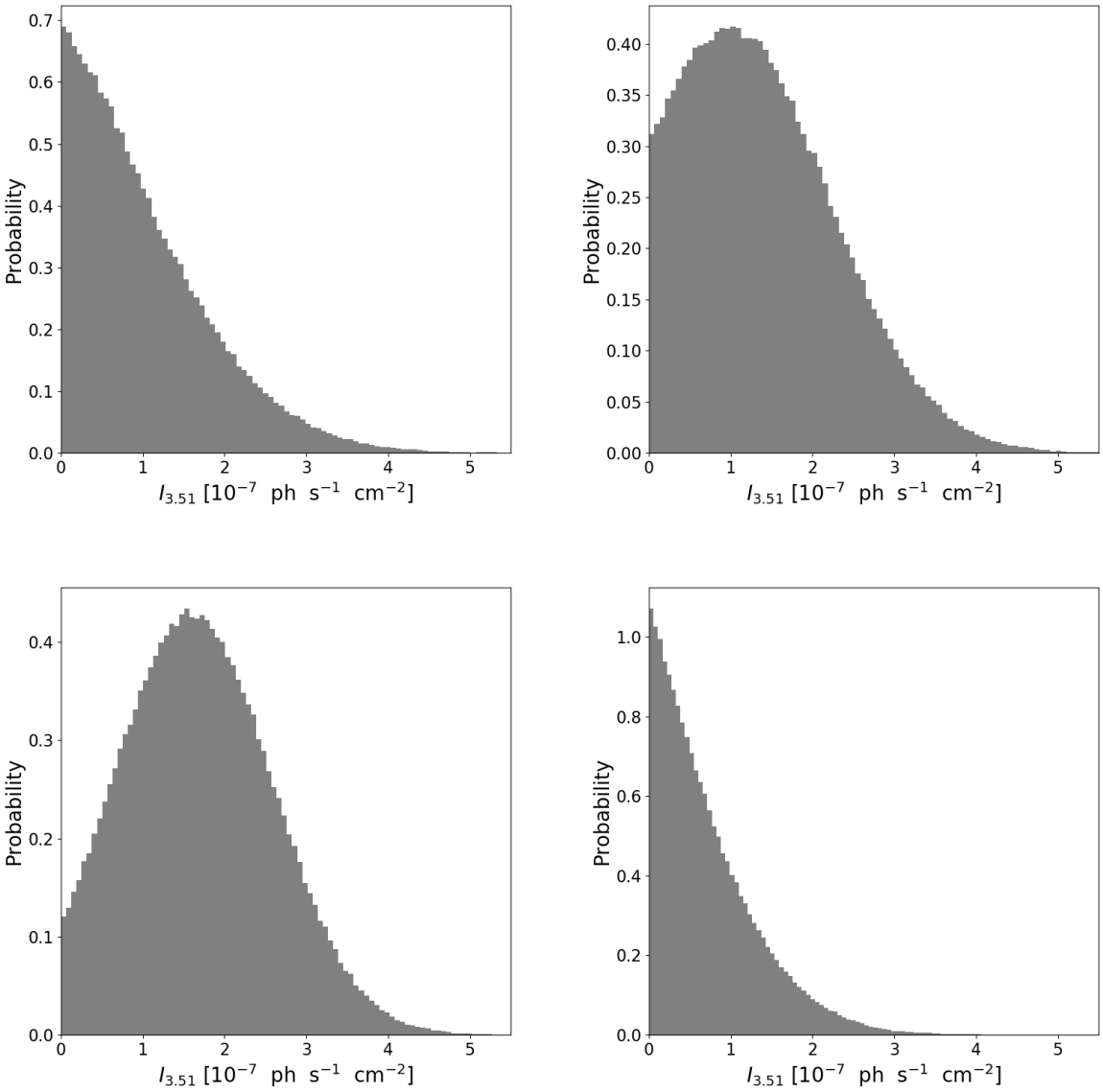


Figure 24. Probability density distributions for 3.51 keV line flux. **Top Left:** Bin 1, **Top Right:** Bin 2, **Bottom Left:** Bin 3, **Bottom Right:** Bin 4.

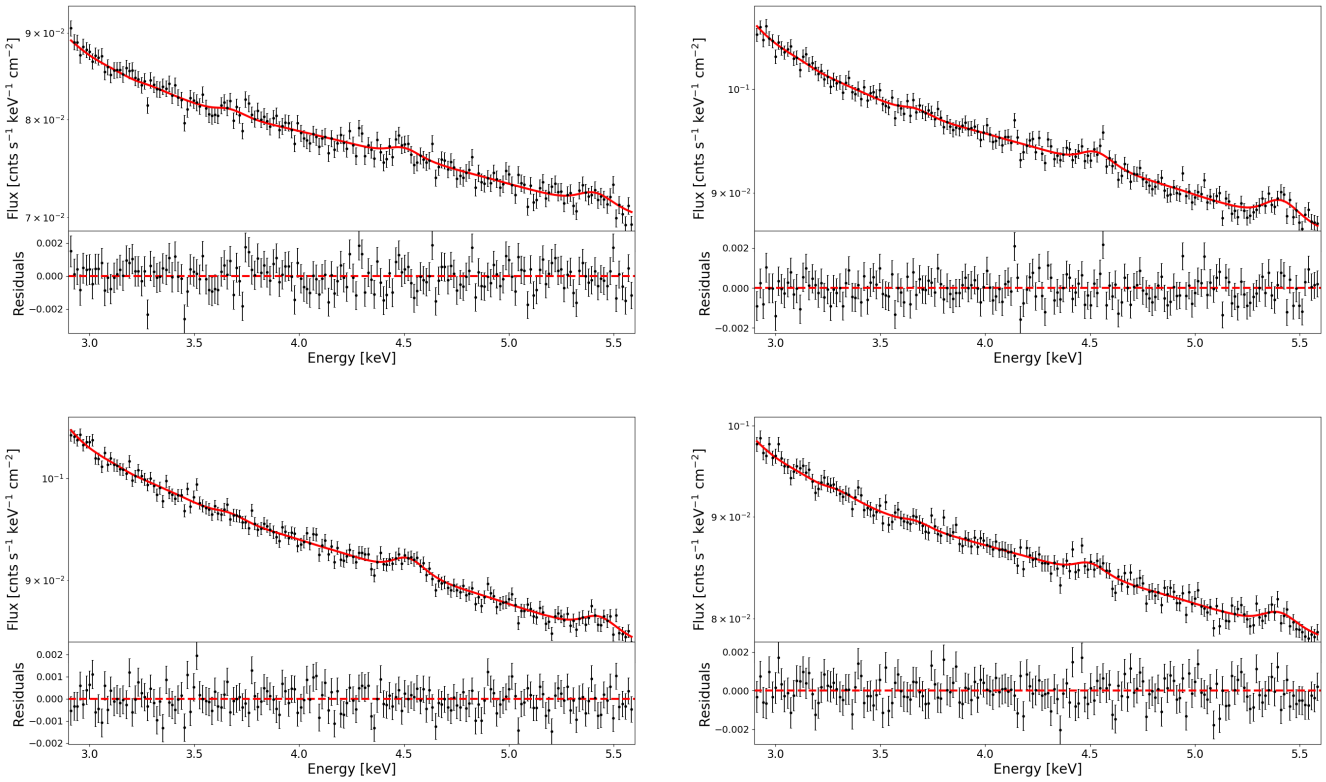


Figure 25. Without removing point-sources: Background-modeled spectra. **Top Left:** Bin 1, **Top Right:** Bin 2, **Bottom Left:** Bin 3, **Bottom Right:** Bin 4.

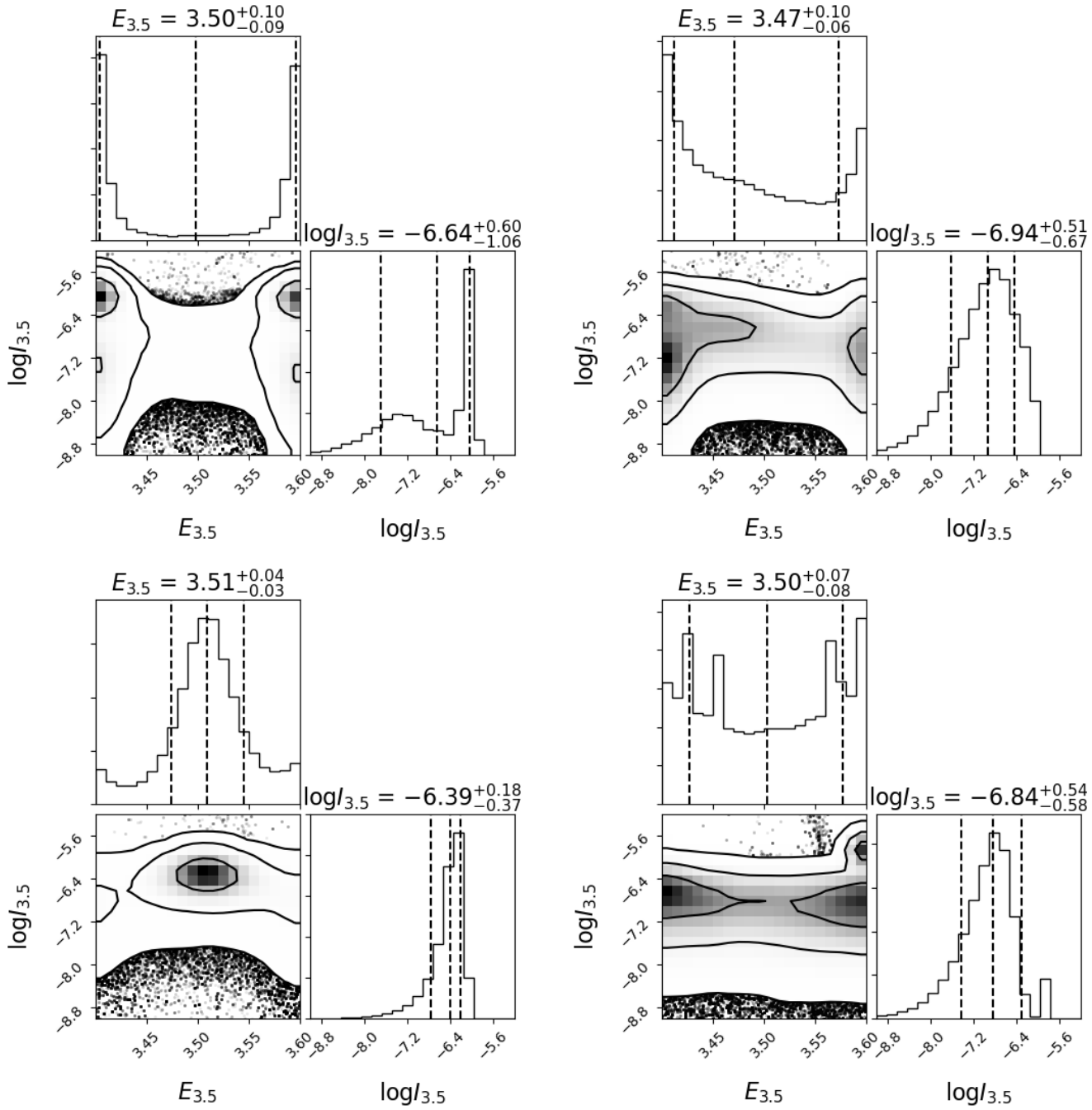


Figure 26. Without removing point-sources: MCMC contour plots for the background-modeled spectra with 3.5 keV line energy free to vary between 3.4–3.6 keV. **Top Left:** Bin 1, **Top Right:** Bin 2, **Bottom Left:** Bin 3, **Bottom Right:** Bin 4.

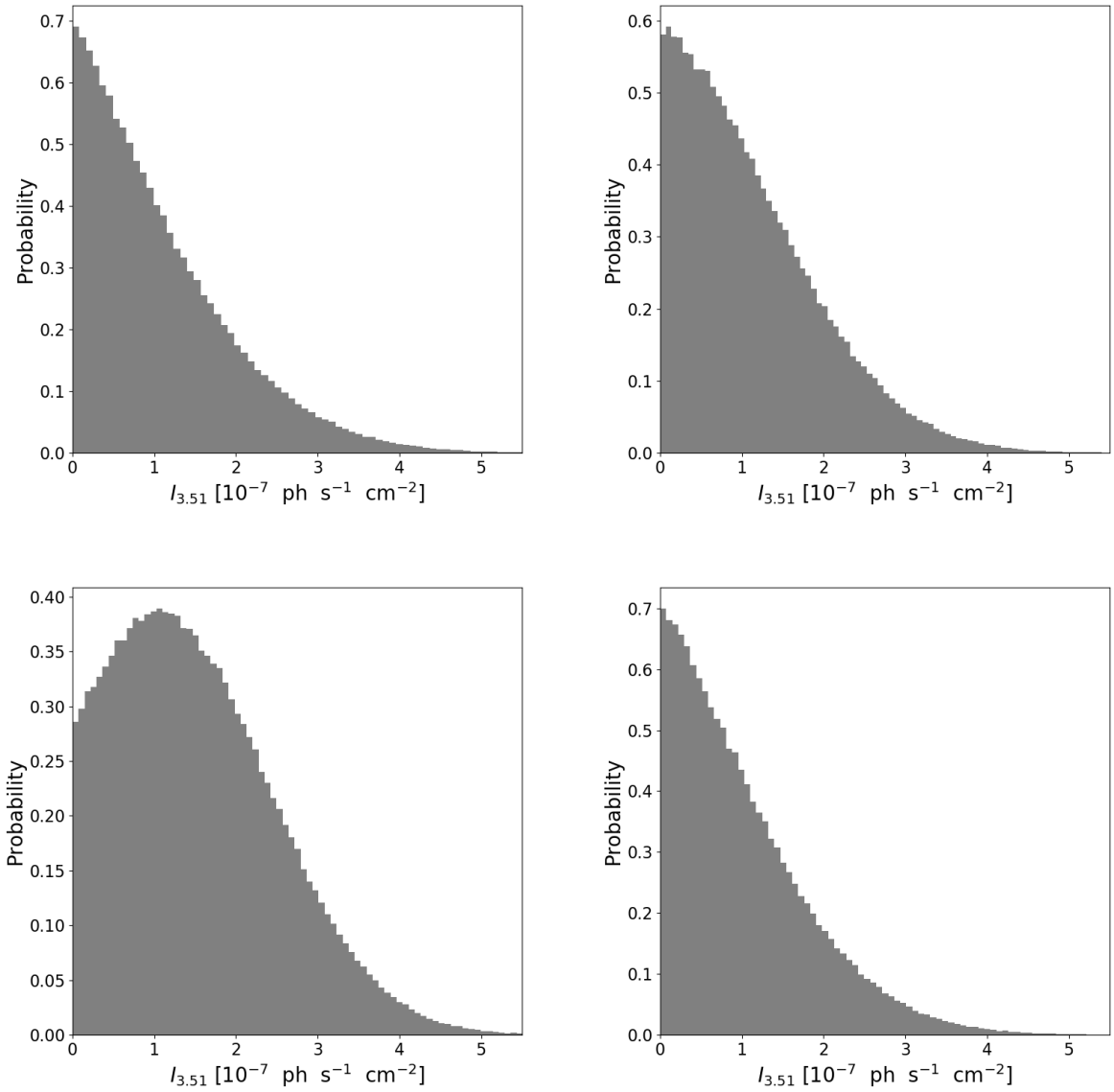


Figure 27. Without removing point-sources: Probability density distributions for 3.51 keV line flux. **Top Left:** Bin 1, **Top Right:** Bin 2, **Bottom Left:** Bin 3, **Bottom Right:** Bin 4.